Charles University in Prague
Faculty of Mathematics and Physics

DIPLOMA THESIS

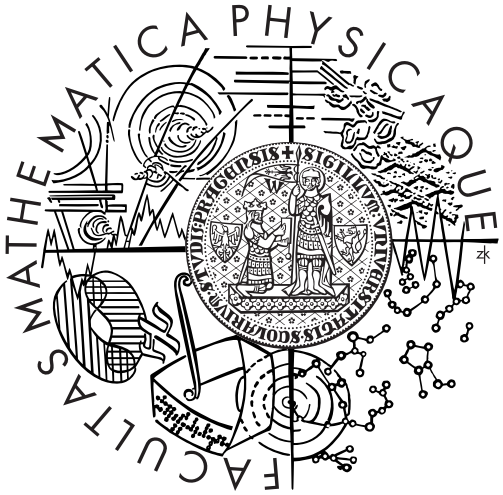

Oldřich Kepka

The QCD analysis of multijet events in proton-antiproton collisions at the Tevatron

April 2006

Institute of Nuclear and Particle Physics
Supervisor: Mgr. Alexander Kupčo, Ph.D.
Field of Study: Physics, Nuclear and Particle Physics

I would like to first thank my advisor Alexander Kupčo for introducing me to the topic of high energy physics analysis, for his tireless help, and support. Also, I'm grateful to Jiří Chýla and Miloš Lokajíček who allowed me to work on the DØ detector at Fermilab in the summer 2005 and the spring 2006. I extend many thanks to Markus Wobisch and Christophe Royon for their openness to answer my questions and also to my teachers at the Institute of Nuclear and Particle Physics. I appreciate Susan Juza's comments concerning my English. Last but not least, I would like to thank my family and my girlfriend for their support and understanding.

I declare that I completed this diploma thesis myself with the use of cited literature only. I agree with using this thesis.

Prague, April 21, 2006 Oldřich Kepka

Contents

Title:	The QCD analysis of multijet events in proton-antiproton collisions at the Tevatron
Author:	Oldřich Kepka
Department:	Institute of Nuclear and Particle Physics
Supervisor:	Mgr. Alexander Kupčo, Ph.D.
Supervisor's e-mail address:	kupco@fzu.cz
Abstract:	The recent developments in theoretical calculations (code NLOJET++) allow us to evaluate the 3-jet observables at the next-to-leading order precision. In this diploma thesis we investigate the potential of using 3-jet observables for the measurement of strong coupling α_s at hadron colliders. First, we analyze the inclusive jet cross section measured by DØ Collaboration, determine α_s and demonstrate its running in a similar way as was previously done by CDF Collaboration. In the second part of the thesis, we analyze the DØ measurement of dijet azimuthal decorrelations. With this choice of 3-jet observable we were able to achieve a better precision of α_s than in the previous α_s measurements based on the inclusive jet production.
Keywords:	strong coupling constant, QCD, multijet events

Název práce:	QCD analýza multijetových případů v proton-antiprotonových srážkách na urychlovači Tevatron
Autor:	Oldřich Kepka
Katedra (ústav):	Ústav částicové a jaderné fyziky
Vedoucí diplomové práce:	Mgr. Alexander Kupčo, Ph.D.
e-mail vedoucího:	kupco@fzu.cz
Abstrakt:	Rozvoj nových výpočetních technik (program NLOJET++) umožnuje počítat produkci tří jetů do druhého řádu poruchové teorie. Naším cílem bylo určit vhodnost takových pozorovatelných pro měření vazebné konstanty silné interakce α_s v hadronových srážkách. Nejdříve jsme se zaměřili na stanovení α_s z měření inclusivního účinného průřezu produkce jetů, které bylo provedeno na experimentu DØ. Druhá část diplomové práce je věnována analýze měření dvou-jetových azimutálních úhlových dekorelací na DØ. Použitím této 3-jetové pozorovatelné se nám podařilo stanovit α_s s lepší přesností než s využitím inklusivního spektra produkce jetů.
Klíčová slova:	vazebná konstanta silné interakce, QCD, multijetové případy

Chapter 1

Introduction

The strong coupling constant α_s is the most fundamental characteristic of strong interaction, and one of the four forces present in the Universe. It is a free parameter of Quantum Chromodynamics (QCD), the theory that describes the interaction of quarks through the exchange of eight color mediators called gluons. QCD is a part of a well established Standard Model, a compound set of theoretical rules which summarizes our contemporary knowledge about the interaction of particles.

The strong coupling has a very interesting characteristic. It evolves as a function of momentum. This evolution is predicted by QCD; however, the particular value of the coupling for a given value of momentum transfer Q^2, cannot be theoretically determined and must be obtained from the experiment. In order to compare extracted values of α_s from various experiments, the widely agreed convention to quote the value at certain momentum scale was accepted. The particular choice of the scale is the mass of Z^0 boson $\mathrm{M}_Z = 91.187\,\mathrm{GeV}$.

In general, α_s is measured in processes involving incoming and/or outgoing quarks and gluons which are observed as hadrons. Since quarks and gluons are never seen isolated in nature, they are confined within hadrons. The combination of α_s fits from numerous experiments is denoted as the *world average*. The up-to-date world average can be found in [1] and reads

$$\alpha_s(M_Z) = 0.1176 \pm 0.0020. \tag{1.1}$$

The error is dominated by the theoretical uncertainties due to the renormalization/factorization scale, parton distribution functions, hadronization models involved etc.

Examples of processes which can be used to evaluate the couping α_s are deep inelastic lepton-nucleon scattering (DIS), electron-positron e^+e^- annihilation, hadron-hadron collisions etc. Their overview is depicted in the Fig. 1.1 [1]. The determination of α_s in hadron-hadron collisions is less precise than in e^+e^- annihilation or DIS. This is due to the major uncertainty associated with the parton distribution functions of the two incoming hadrons.

To illustrate the difference we present the global α_s fit of LEP[1] data (hadronic event

[1]Large Electron and Positron collider at CERN, Geneva

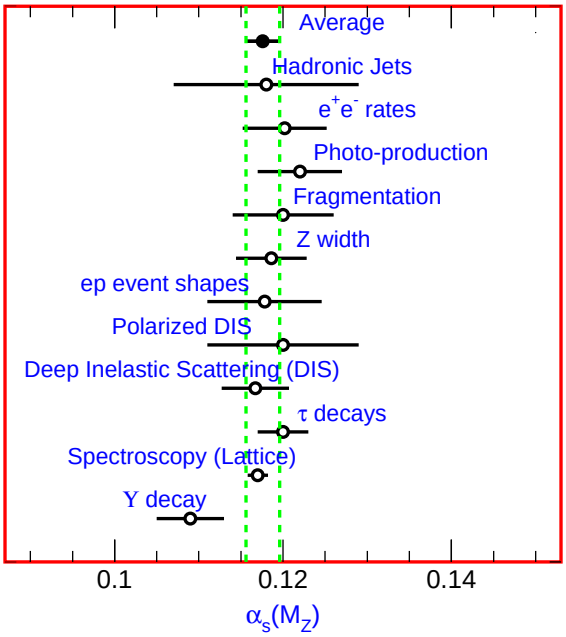

Figure 1.1: Values of α_s evaluated at the scale $\mu = M_Z$ in various processes. The solid lines represent the total error. The dashed band corresponds to the world average, from [1].

shapes, jet production rates in e^+e^-) [2], [3]

$$\alpha_s(M_{Z^0}) = 0.1202 \pm 0.0003(stat.) \pm 0.0049(syst.). \tag{1.2}$$

and the CDF[2] α_s measurement obtained from an inclusive jet cross section [4]

$$\alpha_s(M_{Z^0}) = 0.1178 \pm 0.0001(stat)^{+0.0081}_{-0.0095}(exp.syst) \pm 5\%(theoret). \tag{1.3}$$

Note that in case of the LEP measurement, there are experimental plus the theoretical uncertainties included in systematics . The latter measurement was performed in $p\bar{p}$ collisions at the Tevatron and is the only measurement from the inclusive jet cross section included in the world average. It is obvious that the α_s analysis in hadron collisions is more than by a factor of two less precise than that from e^+e^- experiment.

Running of the coupling constant is tested by evaluating α_s at the scale where it is measured. The collection of α_s obtained from various experiments is seen in Fig. 1.2, inevitably showing the decrease of the coupling constant as a function of the momentum scale.

Although the measurements in collisions involving hadrons are less competitive with LEP, one may hope to improve the precision of α_s determination when advancing to higher orders of perturbative QCD. This is not only because the renormalization scale dependence

[2]Colider Detector at Fermilab, Illinois

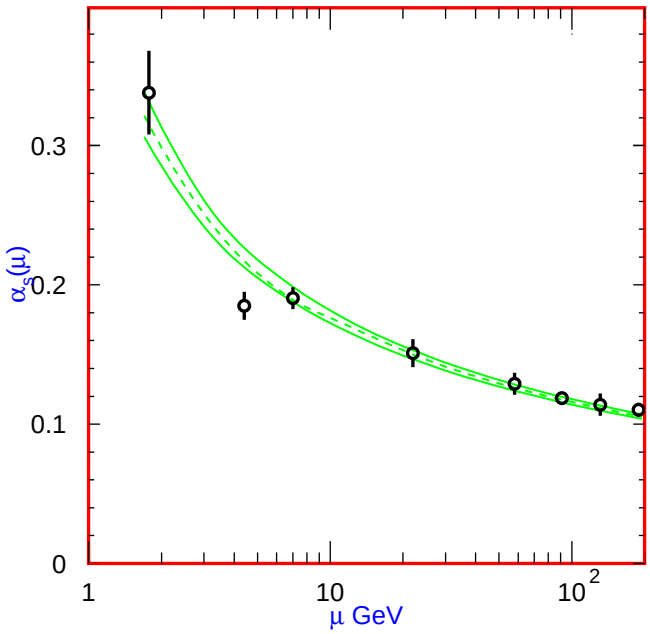

Figure 1.2: Running of the coupling constant α_s as a function of the momentum scale μ. The lines show the central value and the $\pm 1\sigma$ limits of the world average. The running coupling constant decreases as the scale μ increases. The data are, in increasing order of μ, τ width, Υ decays, deep inelastic scattering, e^+e^- event shapes at 22 GeV from the JADE data, shapes at TRISTAN at 58 GeV, Z^0 width, and e^+e^- event shapes at 135 and 189 GeV, from [1].

might be reduced when more terms from higher orders are included. The main improvement is the possibility to construct more appropriate observables which are less sensitive to parton distribution functions and to the experimental systematic uncertainties. In fact, a non-existence of the theory which could have been used to study multijet-observables is the reason why there has been so far only one pure hadronic measurement of α_s.

In the year 2001, a new parton-level Monte Carlo generator for hadron collisions called NLOJET++ was presented [5]. It is capable to calculate not only by now common 2-jet observables but also to provide a prediction for 3-jet observables, both in the next-to-leading order (NLO). With this tool, new multi-jet observables might be calculated. The main purpose of this thesis is to use this technique for the determination of α_s. More specifically, for this we investigate the potential of the dijet azimuthal decorrelation measurement [6] performed by DØ[3].

The theoretical calculation of hadron processes to be compared with the data is extremely time consuming. There has been an attempt to speed up the calculation procedure which led to the development of a new interface so-called fastNLO. It is basically an addition to the NLOJET++ generator, but it can flexibly give a theoretical prediction for any

[3]DØ Experiment at Fermilab, Illinois

choice of the coupling constant and the parton distribution function.

In Chapter 2 we give a short overview of particle physics history. The description of basic characteristics of QCD is summarized in Chapter 3. Computation techniques used in our analysis are introduced in Chapter 4. Chapter 5 is devoted to the calculation of the inclusive jet cross section in NLO to be compared with the DØmeasurement [7]. We extract $\alpha_s(M_Z)$ and study the evolution of running coupling constant as a function of momentum. In Chapter 6, we determine the coupling constant from the measurement of dijet angular decorrelation.

Throughout the thesis we adopt natural units: $\hbar = c = 1$.

Chapter 2

Particle Physics Overview

Physics, or sometimes called Natural Science, is a field of human activity which aims to describe, and deeply understand the diverse behavior of nature. Such a complexity led physicists to divide this field into great number of miscellaneous disciplines each focusing on a specific behavior of nature. Particle physics has the unequivocal position among other disciplines since its main goal is to find and precisely describe fundamental building blocks of matter as well as their mutual interaction.

Since an early age in human history, people have put a great effort into understanding the structure of matter that surrounds them. Their view has undergone many changes; many ideas were developed but later denied as humans compared prediction of plausible theories with real observation of nature.

The general idea that things around us are made of smaller building blocks is not new. Candidates for the role of such fundamental constituents were introduced by the Greek philosopher Democritus of Abdera as abstract invisible particles, or atoms. This revolutionary thought seemed unnatural at that time; however with a progress made more than two thousand years later in thermodynamics and subsequently in atomic and subatomic physics people realized that such a scheme is the correct one, the one realized in nature. It is interesting to note that in this rudimentary attempt it was always much easier to come up with a new building block of matter than explaining what mechanism is responsible for holding the constituents together and thus yielding everything else.

The discovery of an electron yielded the Thomson atom model which describes the atom as electrons confined in a jelly like but relatively massive distribution. Later, with the arrival of first scattering experiments pioneered by Ernest Rutherford, different kinds of atoms were understood as objects with a compact and dense core which is surrounded by a cloud of electrons orbiting around the central kernel. The simplest atom is hydrogen atom whose core is made up of one proton, having the one shell electron orbiting around it.

The rapid progress in particle physics in the 20th century led to by now a well-confirmed picture of fundamental building blocks of matter and energy. Constituents of matter are *fermions* (*leptons* and *quarks*) while *bosons* are corpuscles that carry out the interaction, and are responsible for holding pieces of matter together. An image of the universe that we

see today can be more or less described as a consequence of the existence of such elementary particles.

The lightest charged member of the lepton family is an electron, a particle whose characteristics have been studied in great detail for over one hundred years now. The electron is considered not to have any substructure. Such an assumption agrees with up-to-date experimental observations which probed the electron down to the scale 10^{-18} m and found no electron compositeness [1]. The electron carries negative electric charge. This property stipulates the strength of the interaction between electrically charged objects. With the electron, there comes two additional negatively charged leptons, muon (μ) and tau (τ). The first one is about 200 times heavier, whereas the second is about 4000 times heavier particles than of the single electron. Their significantly bigger mass than of the electron (plus the existence of the weak interaction to be discussed latter) is the reason why muons and taus do not typically build up an atom with protons and neutrons. They decay quickly to the lighter electron. All leptons have antimatter counterparts that have the same mass but positive charge. Adding up positively and negatively electrically charged objects results in entity with null electric charge.

Besides charged leptons, there are three types of neutrinos (ν_e, ν_μ, ν_τ). They do not carry any electric charge. The main characteristic of neutrinos is their inability to interact with almost anything – easily penetrating a large bulk of material such as the entire earth. For many decades, it was believed that neutrinos travel with the maximum possible speed, speed of light and that they are massless. Experiments from the last decade, however inevitably demonstrated that they show nonzero, but rather small mass [1].

The protons and neutrons that build up observed atoms were found not to be the final elementary constituents; their substructure was revealed in experiments performed in the second half of 20th century. Protons and neutrons as well as all hadrons have fundamental subelements which are denoted as quarks and gluons. They interact via the so-called strong interaction.

Quarks come with six different *flavors*. Up (u), down (d), strange (s), charm (c), bottom (b), and top (t). Quarks show no substructure down to the currently smallest probed distance of 10^{-19} m. They carry a fractional electric charge which is expressed in units of electron charge, so they are allowed to interact via electromagnetic force.

In addition, they also have another type of charge, which was named color. It is the color that allows quarks to interact via the strong interaction. Every color has an *anticolor* associated with it. When both colors are mixed together, a color-neutral state or equivalently a white state, is obtained in analogy to a combination of positive and negative electric charge. Moreover, when putting all the three colors together we also arrive with a state which is color-neutral.

The strong interaction has one intriguing property. It mixes quarks to produce particles to be observed in nature in such a way that only white states are created. This phenomenon called *color confinement* makes the determination of quark and strong force properties more intricate.

Let us turn our attention to particles that are responsible for mutual interaction between quarks and leptons. Bosons or precisely gauge bosons, a name whose origin will become evident in an oncoming chapter, play the role of mediators of interactions between

fermions. Currently we distinguish four different fundamental interactions: the electromagnetic, gravitational, weak, and strong force.

A *photon* is the carrier of electromagnetic force. In fact, we experience consequences of electromagnetic interaction every day. A classical description of electromagnetism was presented by James Clark Maxwell in the 19th century in his famous Maxwell equations. He showed that electricity and magnetism are intertwined together and represent two forms of electromagnetism. From his work followed that photons mediating electromagnetic force do not travel with arbitrary high speed, as was not evident at that time. This maximal speed $3.10^8\,\mathrm{m.s^{-1}}$ which any real object cannot exceed is very high in comparison to velocities experienced in regular life.

Attempts in understanding electromagnetism, mainly the studies of the black body radiation, played a crucial role in developing the new concept of physics – *quantum physics*. It basically states that energy and also other characteristics of matter are radiated discontinuously, in small packages, in quanta. In electromagnetism, the quanta are massless bosons (photons) mediating the electromagnetic force to infinite distances.

The second very well studied force is the gravitational one. It acts between massive and massless objects. It is propagated to the infinite distances. Even though general relativity finely describes gravitational behavior of very massive objects in the universe, its quantized version is still missing. It is presumed to be mediated by a massless particle called *graviton*.

The weak interaction is short-range only. It is mediated by massive charged $W^{\pm}$ bosons and electrically neutral Z^0 boson. Effects of the weak force was first seen in at that time mysterious β decay at the beginning of the 20th century. The experimental confirmation of $W^{\pm}$ and Z^0 came much later. In 1983, enough supporting evidence had been gathered for the conclusion that they are produced in the SPS experiment at CERN[1].

Strong force is also a discovery of the last century. Eight particles which carry the strong interaction are *gluons*. Unlike the photon which does not possess a charge of the interaction that it mediates, the gluons do. They have the strong charge, a color, which allows gluons to interact with themselves. They are as elusive as quarks, i.e. they cannot be observed isolated in nature, but are bound forever in hadrons. The appearance of particle showers mainly made of hadrons, that could not be initiated by quarks because of the charge conservation, supported the evidence for gluons. Moreover, quarks inside for example the proton do not altogether carry the entire momentum of the proton. One half of the momentum is carried by other electrically non-charged objects, by gluons. Bounded quarks and gluons inside hadrons are generally denoted as *partons* and identified as the constituents of hadrons.

As all the four forces appear in the current days as forces of a different origin, they are believed to be components of one particular unified force. Although the theoretical unification of three out of four fundamental forces (electromagnetic, weak, and strong) has been already accomplished, the inclusion of the gravitational force still awaits for future development. Because of the large difference in the coupling strength of strong and electroweak interaction, the unification would not be apparent until the energy scale of $10^{14}\,\mathrm{GeV}$ was reached, corresponding to the distance of $10^{-30}\,\mathrm{m}$ [8].

[1] Conseil Européen pour la Recherche Nucléaire, Geneva

Chapter 3

Theoretical Prelude

In this chapter, we provide some historical facts about Quantum Chromodynamics (QCD). A few experiments that gave support to this theory will be stated here. Also, basic aspects of renormalization which introduces running of the coupling constant α_s shall be discussed. The appearance of other divergences when one evaluates Feynman diagrams with an additional parton radiation, the so-called infrared divergences, will be mentioned here. At the end of this chapter, we review the characteristics of parton distribution functions that describe the structure of hadrons.

3.1 Hints for QCD

The proliferation of new experiments to study the strong, weak and electromagnetic properties of particles, resulted with the picture of a great number of newly discovered hadrons. It was very hard to believe that all found species would play a role of truly fundamental particles and be devoid of structure. It was desired to classify the hadrons, to find some higher symmetry that would yield the picture of observed hadron spectrum. Gell-Mann, Ne'eman and Zweig pointed out that the observed mezons and baryons with the same spin and parity can be grouped together [8]. This classification appeared similar to some $SU(3)$ irreducible representation, more concretely the mezons were grouped into octets, while light hadrons into an octet and heavy hadrons into a decuplet. These representations can be expressed as the direct product of fundamental representation of $SU(3)$.

The idea of introducing quarks was thus to have a manifestation for $SU(3)_f$ flavor symmetry which was appearing in the observation of light hadron spectrum. Arranging quarks with spin one half and non-integer electric charge to form totally symmetrical states in a flavor space, it was possible to predict the static properties of other observed hadrons with a surprising precision. For example, with the knowledge of magnetic moment of just three baryons one could compute the magnetic moments of other baryonic states. However, baryons with the spin $\frac{3}{2}$ have both, space and spin wave functions symmetric and thereby violate the rule of Fermi-Dirac statistics which demands the total antisymmetry of the baryon wave function. To remedy the situation, *color*, an additional degree of freedom

was introduced. The wave function of the baryon is then antisymmetric in color index, $a = 1, 2, 3$. Consequently, it is totally antisymmetric, so as to satisfy the precious Fermi-Dirac rule.

In order to give a satisfactory description of observed mezon and baryon spectra, a new degree of freedom had to be augmented with a condition demanding the existence of color singlets only. In the language of group theory, if the quarks q_a transform according to, for example the fundamental (3×3 unitary matrix) representation of $SU(3)_c$ (where index c denotes the color) and antiquarks $\bar{q}_a$ according to the complex conjugate representation, then one can build two kinds of colorless objects $q_a q^a$ and $\epsilon^{abc} q_a q_b q_c$ which represent mezons and baryons, respectively.

A basic test of QCD is the measurement which determines the ratio R of the electron positron total hadronic cross section

$$\sigma(e^+e^- \to \text{hadrons}),$$

compared to the cross section of point-like similarly charged objects such as a muon pair

$$\sigma(e^+e^- \to \mu^+\mu^-) = \frac{4\pi\alpha_e^2}{3s}, \quad \alpha_e = \frac{e^2}{4\pi}$$

as the function of center of mass energy $\sqrt{s}$. The virtual photon emitted by the annihilation of electron and positron will excite all particle and antiparticle states with total energy smaller than of the photon from a vacuum. At low energy there are only three possible such pairs: u, d, s. The ratio R will then be proportional to the sum square of the quark charges. Since a quark and an antiquark can be produced in three color varieties, we must multiply the above sum by the number of quark colors. Finally, the ratio reads,

$$R = 3\left[\left(\frac{2}{3}\right)^2 + \left(-\frac{1}{3}\right)^2 + \left(-\frac{1}{3}\right)^2\right] = 2. \tag{3.1}$$

Once the center-of-mass energy E_{cms} exceeds approximately 10 GeV, the production of quark pairs b, c (mass of c quark is roughly equal to 1.5 GeV, mass of b quark is roughly 4.5 GeV) becomes possible, hence

$$R = 3\left[2\left(\frac{2}{3}\right)^2 + 3\left(-\frac{1}{3}\right)^2\right] = \frac{11}{3}. \tag{3.2}$$

This ratio dependence as a function of $\sqrt{s}$ was indeed experimentally confirmed.

Quarks were introduced to describe static properties of hadrons. However, the pattern how quarks interact was first explored in deep inelastic scattering processes with large momentum transfer in which a relativistic electron scatters off the proton embraced in material. Such an experiment was performed at SLAC[1]. The measured cross section was

[1]Stanford Linear Accelerator Center, California

revealed to satisfy the *Bjorken scaling*. This correlation pattern between the energy and angular distribution of the scattered electron can be described by the Feynman's *parton model* in which the constituents of hadrons were identified with quarks. At short distances, hadrons can be viewed as composed of almost free point-like spin 1/2 constituent *partons*.

A dubious question was why quarks behave almost like free entities while involved in the scattering with large momentum transfer, but on the other hand, they have never been seen isolated. The answer to this riddle is that the coupling of quarks and gluons is large at large distances so as to confine quarks inside hadrons. Contrary, the coupling is small at high momenta or short distances allowing quarks to behave almost free while scrutinized with a high energetic probe. The last property is called *asymptotic freedom* and is effectively described by QCD, a theory of the strong interaction.

3.2 QCD Lagrangian

In the development of Quantum Electrodynamic (QED) and QCD, *gauge symmetries* played a crucial role. *Global symmetries*, i.e. symmetries which are space-time independent, were for example used to describe the isospin $SU(2)$ symmetry of proton and neutron, or as in the case above of flavor $SU(3)_f$ symmetry which classified the observed hadrons as objects composed of quarks.

One can consider more general transformations which are space-time dependent. They are denoted as *local gauge symmetries* because any space-time point experiences different transformation. Such symmetries may be used to generate dynamics, the *gauge interaction*. For example, taking the Lagrangian of a free Dirac field ψ of mass m

$$\mathcal{L} = \bar{\psi}(i\partial\!\!\!/ - m)\psi, \tag{3.3}$$

and demanding the local abelian gauge invariance $U(1)$ of the Lagrangian, it led us to the introduction of one additional gauge field A_μ. According to the local gauge transformation of the fermion field ψ, the vector field A_μ transforms as

$$\begin{aligned} \psi(x) \to \psi'(x) &= \mathrm{e}^{-i\alpha(x)}\psi(x), \\ A_\mu \to A'_\mu &= A_\mu + \frac{1}{e}\partial_\mu\alpha(x), \end{aligned} \tag{3.4}$$

where e is a free parameter that will be identified with the electric charge. The resulting (local) gauge invariant QED Lagrangian then reads

$$\mathcal{L} = -\frac{1}{4}(F_{\mu\nu})^2 + \bar{\psi}(i\partial\!\!\!/ - m)\psi - e\bar{\psi}\gamma^\mu\psi A_\mu. \tag{3.5}$$

A gauge invariant kinetic term of the vector boson $F_{\mu\nu}$ was introduced in order be able to interpret the field A_μ as a field of massless vector boson. The last term in equation (3.5) represents the interaction of the vector boson with the fermion field and is responsible for the dynamics. The strength of the interaction is controlled by the electric charge e.

This concept can be used to construct also the QCD Lagrangian. The construction must reflect the experimental regularity that hadrons appear in color singlet states only. Hence the coupling must grow at large distances in order to confine partons inside hadrons. Moreover, to be able to explain the asymptotic freedom of the parton model, the coupling must decrease at short distances. It can be proven that the Yang–Mills theories whose Lagrangian is invariant under general non-abelian group are capable to describe both the phenomena of strong interaction [8]. If we assume that only the colorless objects are observable, it suggests that the force between the colored quarks must be color-dependent. Hence the group to be gauged is in case of QCD the color group $SU(3)_c$.

Following the above procedure for colored quark fields ψ_k, demanding the local gauge $SU(3)_c$ invariance of the QCD Lagrangian, it implies the introduction of eight gauge bosons A^a_μ, and one free parameter g, the strong charge. The QCD Lagrangian then reads,

$$\mathcal{L} = -\frac{1}{4}(F^a_{\mu\nu})^2 + \sum_{k=\{flavors\}}^{n_f} \bar{\psi}_k(i\not{D} - m)\psi_k, \tag{3.6}$$

where the index $a = 1 \ldots 8$ runs over the index $SU(3)_c$, k is the flavor index, and n_f denotes the number of flavors

$$q_k : \quad u, d, s, c, b, \ldots . \tag{3.7}$$

The covariant derivative is defined in terms of the matrices t^a_r

$$D_\mu = \partial_\mu - igA^a_\mu t^a_r, \tag{3.8}$$

which satisfy the $SU(3)$ commutation relation (A.6).

The field strength tensor of gluons can be expanded as

$$F^a_{\mu\nu} = \partial_\mu A^a_\nu - \partial_\nu A^a_\mu + gf^{abc}A^b_\mu A^c_\nu. \tag{3.9}$$

The most important feature which distinguishes QCD Lagrangian from the QED one is contained in the last term of equation (3.9). Expanding the square of the field strength we get the prescription how the gauge field interacts with itself. The self-interaction of the gauge field enables us to describe the asymptotic freedom and the color confinement.

Theoretical prediction for various processes is calculated in perturbation theory. We use the Feynman diagrams to describe the topology of a given process. The QCD Lagrangian yields the following diagrams: fermion-boson vertex plus three-gluon and four-gluon vertices that are summarized in Appendix A.

Gauge theories, being gauge invariant, represent systems with constrained dynamical variables. There are variables that do not represent true degrees of freedom. The quantization procedure is more complicated in this case. One has to remove these additional degrees of freedom by some acceptable gauge fixing condition. In some gauges the particular gauge fixing condition leads to the introduction of unphysical fields, so-called ghost fields that remove the contribution of redundant degrees of freedom.

3.3 UV Divergences, Renormalization

An application of Feynman rules to compute scattering amplitudes for a given process at the leading order is mostly straightforward. However, when advancing to higher orders of perturbation theory in the coupling $\alpha_s = g^2/4\pi$, one must inevitably deal with Feynman diagrams that contain fermion or boson loops. An evaluation of such diagrams very often leads to an integration over arbitrary large momentum since in the relativistic theory there is no intrinsic cut-off on the momentum present. The theory predicts infinite cross sections and is incapable to describe real processes. Such divergences are denoted as UV divergences for their origin in integration over an ultra-high momentum.

The renormalization is a prescription that allows us to isolate the divergences, and remove all of them consistently from the physically measurable quantities. This introduces an additional mass scale μ - the point where the subtractions which remove the divergent terms are performed. The renormalization leads to the redefinition of the bare quantities which are part of the QCD Lagrangian such as a coupling constant α_s, fermion masses m, the fermion ψ_k and boson A^μ fields, thus introducing their renormalized counterparts. Renormalized quantities are physically relevant, whereas the bare ones are not.

Consider a dimensionless physical observable R which depends on large momentum Q, larger than any other mass m involved. Since the observable is dimensionless, it can depend on the ratio Q^2/μ^2 and the coupling α_s only after the process of renormalization. But the point μ where the subtraction of infinite terms takes place is arbitrary. Hence,

$$\mu^2 \frac{\mathrm{d}}{\mathrm{d}\mu^2} R\left(\frac{Q^2}{\mu^2}, \alpha_s\right) = \left[\mu^2 \frac{\partial}{\partial \mu^2} + \mu^2 \frac{\partial \alpha_s}{\partial \mu^2} \frac{\partial}{\partial \alpha_s}\right] R = 0. \tag{3.10}$$

By introducing new variables τ and β

$$\tau \equiv \ln\left(\frac{Q^2}{\mu^2}\right), \quad \beta(\alpha_s) \equiv \mu^2 \frac{\partial \alpha_s}{\partial \mu^2}, \tag{3.11}$$

we can rewrite the above equation (3.10) as

$$\left[-\frac{\partial}{\partial \tau} + \beta(\alpha_s) \frac{\partial}{\partial \alpha_s}\right] R = 0. \tag{3.12}$$

The above relation is a special case of *Callan-Symanzik* equations generally asserting that for any of Green's function there exist universal functions depending on the coupling constant only (in our case $\beta(\alpha_s)$) related to the shift in the coupling and the field strength, that compensates for the shift in the renormalization scale [10].

The last equation (3.12) is solved by defining a running coupling $\alpha_s(Q)$:

$$\tau = \int_{\alpha_s}^{\alpha_s(Q)} \frac{\mathrm{d}x}{\beta(x)}, \quad \alpha_s(\mu) \equiv \alpha_s, \tag{3.13}$$

where the second equation specifies the initial condition. Differentiating the last equation we obtain the *renormalization group (RG) equation*

$$\frac{\partial \alpha_s(Q)}{\partial \ln(Q^2/\mu^2)} = \beta(\alpha_s(Q)) \tag{3.14}$$

which describes the rate of change of the coupling constant as a function of the momentum Q.

3.4 Beta Function and α_s Running

As we will demonstrate, QCD is an asymptotically free theory which means that the coupling $\alpha_s(Q) \to 0$ as $Q \to \infty$. This is the reason why we can safely use a perturbation theory for large Q. Including diagrams with one fermion or boson loop, the β function perturbative expansion in α_s reads

$$\beta(\alpha_s) = -b\alpha_s^2 + \mathcal{O}(\alpha_s^3), \tag{3.15}$$

where for a general non-abelian group $SU(N)_c$ the leading coefficient is

$$b = \frac{1}{4\pi}\left[\frac{11}{3}C_2(A) - \frac{4}{3}n_f C(F)\right]. \tag{3.16}$$

$C_2(A)$ is a Casimir operator of the adjoint representation A (A.11), and $C(F)$ is the normalization coefficient for the generators of the group in fundamental representation F (A.8), and n_f is a number of active flavors. If the number of flavors is sufficiently small, $\beta(g)$ is negative. We see that non-abelian theories are able to describe asymptotic freedom, driving the renormalized coupling to zero when the momentum increases. For the three color $SU(3)_c$ group, the coefficient b takes the form

$$b = \frac{33 - 2n_f}{12\pi}. \tag{3.17}$$

The solution of the renormalization group equation (3.14) can be written as

$$\alpha_s(Q) = \frac{\alpha_s(\mu)}{1 + \alpha_s(\mu)b\tau}, \quad \tau = \ln\left(\frac{Q^2}{\mu^2}\right). \tag{3.18}$$

The sign of b is very important. In QCD $b > 0$, therefore α_s tends to zero as Q becomes large, contrary to QED where $b < 0$ and the coupling increases as Q grows.

Let us explicitly write down, mainly for the reference reasons, the solution in the case of two-loop approximation. Considering the $SU(N)_c$ group as the symmetry group of QCD Lagrangian, the β function reads [11]

$$\beta(\alpha_s) = -b\alpha_s^2(1 + b'\alpha_s) + \mathcal{O}(\alpha_s^4), \tag{3.19}$$

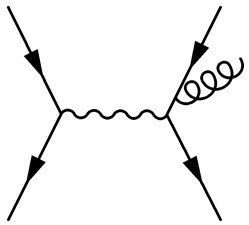

Figure 3.1a: LO Feynman diagram for the $e^+e^- \to \bar{q}qg$ process

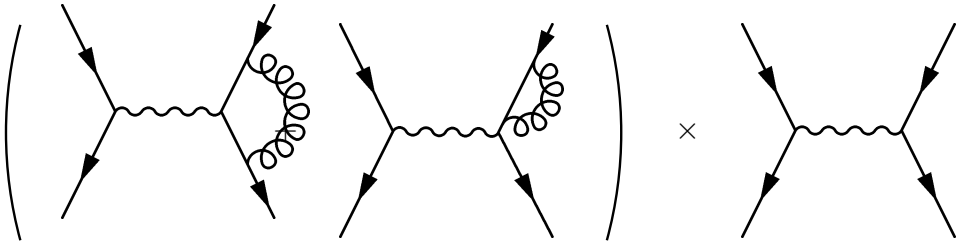

Figure 3.1b: The two interference terms contributing to the process $e^+e^- \to$ hadrons at the order $\mathcal{O}(\alpha_s)$.

with

$$\begin{aligned} b &= \frac{11C_2(A) - 2n_f}{12\pi} = \frac{33 - 2n_f}{12\pi}, \\ b' &= \frac{17C_2^2(A) - 5C_2(A)n_f - 3C_2(F)n_f}{2\pi(11C_2(A) - 2n_f)} = \frac{153 - 19n_f}{2\pi(33 - 2n_f)}. \end{aligned}$$

The solution of the RG equation at the two-loop approximation can be then written as

$$\alpha_s(Q) = \frac{\alpha_s(\mu)}{1 + b\alpha_s(\mu)(1 + b'\alpha_s)\tau}, \quad \tau = \ln\left(\frac{Q^2}{\mu^2}\right). \tag{3.20}$$

Currently, the β function expansion coefficients have been calculated up to four-loop approximation. One can find additional information in the paper [12].

3.5 IR Divergences

In the quantum field theory containing at least one massless gauge boson such as QCD, one faces an additional ambiguity when predicting certain processes. In particular, imagine the production of a quark antiquark pair in electron positron annihilation with one additional gluon radiated in the final state. Evaluating the diagram Fig. 3.1a at the leading order in

α_s we obtain the following formula for the differential cross section

$$\frac{\mathrm{d}\sigma}{\mathrm{d}x_1\mathrm{d}x_2}(e^+e^- \to \bar{q}qg) = \frac{4\pi\alpha_e^2}{3s}\sum_f 3Q_f^2\frac{\alpha_s}{2\pi}\frac{x_1^2+x_2^2}{(1-x_1)(1-x_2)}, \tag{3.21}$$

where $x_1 = 2E_1/\sqrt{s}$, $x_2 = 2E_2/\sqrt{s}$ are the fractional energies carried by the outgoing quark and antiquark with respect to the center of mass energy, respectively.

For a certain kinematic configuration of the final state, the formula (3.21) gives an infinite cross section. In particular, the singularity at x_1 occurs when the gluon is emitted in the same direction and in parallel to the antiquark. Similarly, the singularity at x_2 appears when the gluon in the final state is parallel to the quark. Finally, the double singularity arises when the radiated real gluon has zero energy. Singularities of this type are denoted as *mass singularities* because the divergence appears due to the vanishing mass of either the gauge boson or the fermion.

The treatment of such divergences is of a different type than in the case of UV divergences. The idea is to take into account not only the Feynman diagram for a specific process, but also include higher order diagrams with virtual bosons. They contain *infrared divergence* (IR) terms due to the integration over the small values of momenta. Such effects are the resemblance of long-distance behavior of the theory, contrary to the UV divergences which were related to short-distance effects and led us to the redefinition of the coupling constant, mass terms of fermions and field strengths of both fields.

The technical tool to attack IR divergences is, for example, to introduce a regulator for the diverging integrals, assuming a non-zero mass of the gauge boson. Summing up the contributions from diagrams that lead to the same final state, or in other words, that are physically indistinguishable, the infrared terms cancel each other. In the example above, the configuration of the collinear gluon that gave birth to the divergences in the formula (3.21) is indistinguishable from states that single quark carries momentum of the gluon-quark pair. It is logical to include diagrams, which contribute to the cross section at the same order as the diagram with real gluon radiation does. Few such diagrams are depicted in Fig. 3.1b. The first diagram exactly cancels the divergent part of the diagram 3.1a, the second gives a contribution to the quark self energy. The total cross section of the process $e^+e^- \to$ hadrons at first order of α_s approximation than reads

$$\sigma_{NLO} = \sigma_{LO}\sum Q_f^2\left(1+\frac{\alpha_s}{\pi}+\mathcal{O}(\alpha_s)\right) \tag{3.22}$$

and is finite. Moreover, formula (3.21) describes well the production of three partons in the final state outside the region of singularities, but cannot be used in the above mentioned case of collinear and soft gluon emission.

In the real experiment, however, it is not possible to detect particles with arbitrary small momentum, nor to "see" the final states where gluons are emitted very close to the quark. The latter case will appear in the detector as a presence of one particle with the total 4-momentum equal to the combination of quark and gluon momenta. It is, therefore, natural to introduce an object that would take such experimental disabilities into account.

We are led to the definition of a *jet*. Partons that are very "close" to each other in a sense that will be discussed in the next chapter, are together represented with a single observable jet. In our example, the collinear gluon and quark will create one jet only and hence effectively represent a single particle to be measured in the detector. This final three-body state is a state with two jets, very similar to the state in which only a quark and an antiquark are emitted. So the introduction of jets for the description of final states resembles our procedure of summing two-parton and three-parton final states above, in order to obtain finite result for the total cross section of $e^+e^- \to$ hadrons (3.22).

The cancellation of infrared divergences to any order of the perturbation expansion is the topic of Kinoshita–Lee–Naunberg theorem. Consider the scattering between initial (I), and final (F) states $I \to F$, containing massive particles. Although the single amplitude of the reaction $S_{F\leftarrow I}$ may suffer from IR divergences, the sum

$$\sum_{D(I)D(F)} |S_{D(F)D(I)}|^2, \tag{3.23}$$

is finite, and this relation holds even when partons are allowed do have nonzero mass [13]. The letter D, denotes states that all have the same conserving quantum numbers and their total 4-momenta are equal, i.e they are physically indistinguishable.

3.6 Parton Distribution Functions

Hadrons are not point-like objects; they are compound of quarks and gluons. The hadron structure is described by parton distribution function (PDF). They are universal. The same function can be used to describe a proton in ep collisions as well as in the processes with two incoming hadrons. This is possible due to the feature of factorization which will be discussed here.

The high-energy interaction of hadrons are described by the QCD parton improved model (pQCD). In this model a hard scattering process is a consequence of an interaction between quarks and gluons which are constituents of the incoming hadrons. The cross section for a hard scattering of two hadrons with their momenta P_1 and P_2 is viewed as the cross section of the two partons and can be written as

$$\sigma(P_1, P_2) = \sum_{i,j} \int \mathrm{d}x_1 \mathrm{d}x_1 \hat{\sigma}_{i,j}(p_1, p_2, \alpha_s(\mu_r^2), Q^2/\mu_r^2, Q^2/\mu_f^2)) \otimes f_i(x_1, \mu_f^2) \otimes f_j(x_1, \mu_f^2). \tag{3.24}$$

The momentum of partons p_1 and p_2 entering the hard interaction varies from event to event, satisfying $p_1 = x_1 P_1$ and $p_2 = x_2 P_2$. The characteristic momentum scale Q can be the transverse momentum of a jet in the final state. The functions $f_i(x, \mu_f^2)$ are QCD quark and gluon distribution functions, defined at a factorization scale μ_f. They describe the probability to find a parton of type i within the hadron, carrying the hadron momentum fraction x. The short-distance cross section for the scattering of partons of type i, j is

denoted by $\hat{\sigma}_{i,j}$. It can be calculated as a perturbation series in the running coupling constant α_s, because the coupling is small at high energy. The (n+k)th-order approximation to the short-distance cross section is given by

$$\hat{\sigma} = \alpha_s^k \sum_{m=0}^{n} c^{(m)} \alpha_s^m, \tag{3.25}$$

where the $c^{(m)}$ perturbative expansion coefficients are functions of the kinematic variables and the renormalization and factorization scales. Different hard processes will contribute with the different leading powers k. For example, the jet production at large p_T has $k = 2$.

In the leading approximation to a given process, where $n = 0$ the short-distance partonic cross section is calculated in the usual way as for any tree-level process. In higher orders, the short-distance partonic cross section is obtained from the partonic cross section by removing long-distance terms and factorizing them into the PDF. This is needed because the perturbatively calculated cross section comprises effects that occur long before the hard scattering. Factorizing the long-distance terms into the distribution functions, the short-distance perturbative cross section depends on the physics with a high transverse momentum only. It is not sensitive to the details of the hadron wave function or the type of the incoming hadron but is a purely perturbative short-distance matter.

The *factorization scale* μ_f can be thought as the divider between short-distance and long-distance effects. The parton emitted with a small transverse momentum less than the scale μ_f is considered part of the hadron structure and is absorbed into the definition of the parton distribution function. On the other hand, a parton emitted at large transverse momentum contributes to the short-distance cross section.

The renormalization scale μ_f is an arbitrary parameter. The cross section evaluated to all orders, as in the case of the renormalization scale, does not depend on this scale

$$\frac{\partial \sigma}{\partial \mu_r} = \frac{\partial \sigma}{\partial \mu_f} = 0. \tag{3.26}$$

However, the truncated perturbative expansion generally does depend on the choice of the scale. The simplifying assumption of a single scale $\mu = \mu_r = \mu_f$ is often made and the standard choice is $\mu = Q$, where Q is the hard scattering scale.

The PDF evolution on the scale variable is described by the *Dokshitzer-Gribov-Lipatov-Alltarelli-Parisi* (DGLAP) differential evolution equations. Specifying the PDF at some arbitrary scale μ_0 (initial condition), one can evolve the PDF to and arbitrary momentum value μ_f by solving the DGLAP equations. The initial condition, however, cannot be perturbatively computed from the first principle out of the QCD Lagrangian, but must be obtained from the experiment. This is done by fitting the distribution functions to the real measured cross sections. One parameterizes the quark and gluon PDFs of a hadron by a set of parameters, than evolves the distribution function using DGLAP to the required scale relevant for a particular process and make a theoretical prediction to be compared with the data.

In this thesis we predominantly use the CTEQ parameterization of the PDF. In the set version CTEQ6.1M, the group presented not only the PDF itself, but also provided distribution function to study the uncertainty on the global PDF fit [9]. They can be used to evaluate the total theoretical uncertainty originating in PDFs on a given observable.

There are forty-one PDFs denoted as $S_0,\ S_1^+,\ S_1^-, \ldots S_{20}^+,\ S_{20}^-$. The PDF S_0 is the so-called central value and corresponds to the best fit. The remaining forty functions correspond to the shift in twenty independent parameters along the eigen vectors of the Hessian matrix in both directions. The uncertainty ΔX on the variable X is then computed with the following formula

$$(\Delta X)^2 = \sum_{i=1}^{20} \left[\frac{X(S_i^+) - X(S_i^-)}{2} \right]^2 . \tag{3.27}$$

Chapter 4

Program Interface

In the previous chapter we mentioned the significance of using jets as a tool to study the QCD properties. First, we will define a jet, using the jet cone algorithm. Then a brief survey of Monte Carlo generators used for our analysis of two measurements performed at Tevatron follows.

4.1 Jet Cone Algorithms

In Chapter 2 we justified the concept of a jet which was built up from partons that emerged from the hard interaction. Using jets we were able to comprise the effects of physically indistinguishable states and get rid of the IR divergences. Their definition is motivated with one more argument. In hadron scattering, we usually have one or more outgoing partons with large transverse momentum p_{T} (transverse to the direction of incoming hadrons) and remnants of the hadrons traveling in the direction of collided hadrons. Free partons are never seen isolated and the outgoing partons tend to fragment or hadronize to form color singlet hadrons. The mutual interaction between outgoing partons as well as the interaction of outgoing partons with hadron remnants forcing color objects to hadronize is very soft. It occurs over long distances, with a small momentum transfer, much later after the hard scattering. Since α_s is large for small momentum, these effects cannot be understood from the perturbative theory point of view but are described by phenomenological models such as model of independent fragmentation [13] or Lund string model. However, because the exchanged momentum is relatively small in comparison to the momentum of outgoing parton, we assume that the kinematic properties of partons are not greatly affected by hadronization when moving away from the interaction point. Hence the spray of particles travels approximately in the direction of the outgoing parton.

Jets can be defined generally on three different layers. First, we define a *parton jet* that are build up of partons. They are used in fixed order perturbative QCD calculation. Secondly, we define *hadron jets* at the hadron level, i.e. jets are constructed from particles obtained in the Monte Carlo simulation of the particular process. Lastly, we define *detector jets* on the detector level. The smallest active detection object in the calorimeter (most of

the information for jet reconstruction comes from the calorimeter) is called a cell. They are usually arranged into calorimeter towers in such a way to follow as much as possible the path of particles escaping from the interaction point. The detector jets are composed of calorimeter towers. The most important demanded jet property is the high correlation between jets calculated at different levels. This gives the desired possibility to compare predictions of perturbative QCD with the measured jet observable.

There is not a unique method of how to define jets. The particular way how to construct them is called a *jet algorithm*. The ideal jet algorithm should be infrared and collinear safe, i.e. it should be insensitive to the additional emission of a soft parton and to the replacement of a parton by two very close partons carrying in total the same energy as the original parton. The IR safety of the algorithm is crucial for the consistent theoretical prediction. Additional jet radiation in the final state can greatly affect the particular observable on the parton level, whereas its effect is almost negligible at the detector level.

In order to be able to compare the results from various experiments, the jet algorithm should not depend much on the detector characteristics, such as cell size and their segmentation, experimental conditions, i.g. luminosity, detector noise, etc. The algorithm should be straightforward to implement and fast because the off-line jet reconstruction is typically very time consuming.

There is a great number of jet algorithms used in high energy physics. In this thesis we use measurements that were performed with the cone algorithms only, hence only their properties will be discussed. The idea of the cone algorithm is indeed very simple. It creates an exclusive subset of nearby items (on the parton, particle, or detector level) that lie inside a geometrical cone of a radius R. One has to give a particular prescription how to compute the jet properties from the items which where assigned to the jet. This procedure is called a *recombination scheme*.

We will analyze two measurements performed by the DØ collaboration, hence we focus on the description of jet algorithms used there only. The two jet algorithms applied at the DØ measurements are Run I and Run II [14] cone algorithms. In the Run I algorithm, jets are described by three variables: the azimuthal angle ϕ drawn in the plane perpendicular to the beam axis, the polar angle θ between the direction of the jet and the beam axis, and the transverse energy of the jet E_T. The latter angle is connected to the *pseudorapidity* η satisfying the relations

$$\eta = -\ln\tan\left(\frac{\theta}{2}\right) = \frac{1}{2}\ln\left(\frac{|\vec{p}|+p_z}{|\vec{p}|-p_z}\right). \tag{4.1}$$

$\vec{p}$ and p_z are the momentum and the longitudinal momentum, respectively. The distance between jets is defined as the distance in the abstract $\phi \times \eta$ plane as

$$\Delta R = \sqrt{\Delta^2\phi + \Delta^2\eta}. \tag{4.2}$$

To obtain the jet properties out of its items, *Snowmass* or E_T recombination scheme [15] was implemented in the Run I cone algorithm. The properties of a jet are obtained as

transverse energy E_T weighted sums:

$$E_T^{jet} = \sum_i E_{T_i}, \quad \eta^{jet} = \frac{\sum_i \eta_i E_{T_i}}{\sum_i E_{T_i}}, \quad \phi^{jet} = \frac{\sum_i \phi_i E_{T_i}}{\sum_i E_{T_i}}. \tag{4.3}$$

These definitions preserve the boost invariance of the cone radius along the beam axis naturally. Jets are by definition massless.

Another possibility to obtain the jet characteristics is to sum the 4-momenta of contributing items. This scheme called E-scheme has been used during Run II. Jets are not generally massless, and instead of pseudorapidity η, the true rapidity y

$$y = \frac{1}{2} \ln \left(\frac{E + p_z}{E - p_z} \right), \tag{4.4}$$

is used to determine the distance ΔR between jets

$$\Delta R = \sqrt{\Delta^2 \phi + \Delta^2 y}. \tag{4.5}$$

In case of massless jets the rapidity (4.4) is the psudorapidity η (4.1). The application of a recombination scheme is straightforward at the parton/particle level, one just sums the 4-momenta of partons/particles. At the detector level, the elementary item is a cell whose 4-momentum is determined from the measured energy deposited in the cell E_{cell} and the spatial direction $\vec{n}_{cell}$ from the primary vertex to the cell

$$P_{cell} \equiv E_{cell}(1, \vec{n}_{cell}), \quad |\vec{n}_{cell}| = 1. \tag{4.6}$$

As mentioned above, calorimeter cells are organized into towers,

$$P_{tower} \equiv (E_{tower}, \vec{p}_{tower}) = \sum_{cell} P_{cell}, \tag{4.7}$$

and they serve as the elementary items to build up detector jets

$$P_{jet} \equiv (E_{jet}, \vec{p}_{jet}) = \sum_{tower} P_{tower}, \tag{4.8}$$

The next step is to specify which items contribute to which jet. The jet reconstruction cannot be done analytically, but it is an iterative procedure.

- The algorithm starts from any item (parton, particle, calorimeter tower) and draws a cone of radius $R = R_{cone}$ around it. Adding all the items that lie inside the cone radius, it calculates the new cone direction according the the recombination scheme (4.3) or (4.8). Once again the cone of radius $R = R_{cone}$ is drawn, and the new direction is reevaluated. This procedure is repeated as many times until the new calculated cone direction does not differ from the previous one. This stable solution of the cone algorithm is called a *protojet*.

- After finding all the stable solutions, many protojets overlap. To avoid double counting of energy, the cone algorithm must decide to which jet will the shared particles contribute. The pair of two protojets is merged if they share more then 50% of one of the protojets transverse momentum. In the opposite case, they are split in two distinct protojets. Items which are owned by both of the protojets are assigned to the closest one. After the merging and splitting procedure the direction of the new born protojets is reevaluated using the recombination scheme (4.8). Throwing out the soft protojets that have p_T smaller than some bias leave us with the list of found jets.

The particular value of R_{cone} above is chosen so as to most likely resemble the geometry of real particle spray inside the detector. In our analysis, we use the same value $R_{cone} = 0.7$ as was used in both Run I and Run II cone algorithm by the DØ collaboration. It is shown in [16] that this particular choice of the cone radius minimalizes the renormalization scale dependence of the inclusive dijet mass cross section.

To guarantee the IR safety of the algorithm at parton level (in the theoretical calculation with up to four partons in the final state), midpoints between two protojets are also used as the starting points to search for the stable cone solutions. Imagine two partons which are separated by a distance of almost $2R_{cone}$ in the $\phi \times \eta$ plane. In this situation, the jet cone algorithm would clearly find two distinct jets. Now suppose there is a soft gluon radiated just in between the two partons. The jet reconstruction will end up with just one single jet in the final state, so the algorithm is soft parton emission dependent, hence infrared unsafe.

The midpoint starting position is calculated from the 4-momenta of two protojets P_1, P_2

$$P_{mid} = P_1 + P_2. \tag{4.9}$$

However, only the protojets that are closer than $2R_{cone}$ in distance are considered for midpoints. Only such protojets may possibly create one single jet when the additional soft jet is emitted in between the two. Stable solutions are then found also using the midpoints.

The Run I algorithm did not have the enhancement of midpoints. One can wonder, why it was possible to use such IR unsafe algorithm in data taking. Although it is impossible to use the Run I algorithm for the theoretical calculation, the IR unsafety is not an issue at detector level. The detector event is characterized by a proliferation of particles which leads to energy deposition in a great number of towers. The situation when there are two protojets separated by a distance close to $2R_{cone}$, occurs with very low probability. More often the distance is much smaller. Hence there is always a protojet present between two protojets that takes the role of a midpoint naturally.

Strictly speaking, the difficulty of Run I cone algorithm arises when calculating a theoretical prediction with four and more partons in the final state. In a theory where there are at most three partons in the final state, the Run I algorithm is does not suffer from IR divergences.

4.2 Calculation of QCD Processes

The theoretical evaluation of hard scattering of hadrons (more specifically protons and antiprotons) is rather complex since it comprises the insertion of non-perturbative effects – PDFs, hadronization model, etc. The collisions are simulated event by event in Monte Carlo Generators (MC). The typical event generation can be basically divided into three steps:

1. Initial state hadrons are described by their PDFs which were extracted from many different experiments. According to the probability of a given parton to be found inside the proton with a specific momentum, the parton is chosen to initiate the hard interaction with a parton coming from the antiproton.

2. The hard process of two parton interaction is computed to the specific order in perturbation theory with numerous partons in the final state. In some MC generators multi-parton emission from the final state partons is included in parts of the phase space in order to comprise the higher order perturbation theory effects.

3. Some hadronization model must be applied to transform produced partons into color neutral states. Final state stable hadrons are used to calculate an observable i.e. inclusive dijet mass spectrum, inclusive jet production etc., which is then compared with the measured data.

Pythia [17] is a Monte Carlo generator that is capable to simulate the collisions of particles entirely on parton and particle level. It gives the list of partons before the hard scattering is initiated, after the hard scattering, and after the hadronization. The latter two are of particular interest since it enables the comparison of jet properties and arbitrary observables at the hadron and the parton level.

There are only the leading order (LO) matrix elements considered in Pythia, the S-matrix is proportional to α_s. Higher order effects are simulated in a model of initial and final state additional parton radiation so as to best describe available experimental measurements. We use this MC generator to study the non-perturbative effects on the inclusive jet cross section in the next chapter.

The hard process matrix evaluation beyond LO, up to $2 \to 3$ jet processes at next-to-leading order (NLO), can be obtained with the C++ library NLOJET++ [5]. It proceeds similarly to the above mentioned procedure of hadron scattering, but no multi-parton emission effects or hadronization model are provided. Thus, one is left with the list of final state partons only. It evaluates the particular matrix elements in $\overline{MS}$ renormalization scheme and takes into account the proton/antiproton distribution functions. The application of a specific cone algorithm leads to the prediction of desired parton jet spectra. It is capable to evaluate predictions for ep processes [18] relevant for HERA[1]experiment, and hadron-hadron ($pp, \bar{p}p$) processes [19], [20], [21] significant for the Tevatron, and LHC experiments. For hadron-hadron processes in particular, the calculation is carried out to the accuracy shown in Tab. 4.1.

[1]Hoch Energie Ring Anlage at DESY – Deutsches Elektron–Synchrotron, Hamburg

	$2 \to 2$ jets	$2 \to 3$ jets	$2 \to 4$ jets
LO	α_s^2	α_s^3	α_s^4
NLO	α_s^3	α_s^4	$\times$

Table 4.1: NLOJET++ is able to calculate two- and three-jet observables in hadron-hadron scattering at NLO order, whereas the calculation with four jets is carried out at LO precision only.

The NLOJET++ generator can calculate the prediction for any infrared safe two-, and three-jet observable at NLO. Saying that the calculation comprises $2 \to 3$ jet processes in LO means to calculate all tree-level diagrams with three final state partons. Going to NLO for this process requires to include one fermion and boson $2 \to 2$ loop diagrams which will interfere with $2 \to 2$ tree-level diagram, with the contribution proportional to α_s^3.

This sequence has been already illustrated in Fig. 3.1b. It can also be used to illustrate the case of $2 \to 2$ hadron process if we replace electron, positron, and photon by quark, antiquark, and gluon, respectively, bearing in mind that there are many more possible Feynman diagrams contributing to the hard scattering S-matrix since we can have any pair of $\bar{q}, q, g$ in the initial state as well as in the final state.

From Tab. 4.1 it might look as $2 \to 2\,\text{NLO}$ and $2 \to 3\,\text{LO}$ predictions are the same since they have the same accuracy of α_s. It is deceptive. $2 \to 2\,\text{NLO}$ diagrams contain one loop, but $2 \to 3$ a LO is purely tree-order calculation. Analogically, $2 \to 2\,\text{NNLO}$ would contain two loop diagrams, etc.

4.3 Theory and Data Comparison

In this thesis we make predictions for the inclusive jet and the dijet decorrelation spectrum at NLO with the NLOJET++ generator that calculates jet observables at the parton level. In order to correctly compare theoretical calculation with the experimental measurement at the detector level, it is inevitable to study and apply the hadron-parton correction for a particular cross section. As we stated earlier, the appearance of jets in the detector is an unequivocal fingerprint of a production of partons with high transverse momenta. However, to determine the parameters of QCD such as the coupling constant α_s, one has to take into account even rather small hadronization correction. These effects might be negligible for one observable, but might be of the order of few percent for another. If the measurement of the cross section σ was done as a function of x (i.e. of $p_T, \Delta\phi$, etc.), the full prediction σ_{pred} of the theory for each x bin will be determined as

$$\sigma_{pred}(x) \equiv C_{hp}(x)\sigma_{parton}^{NLO}(x), \quad C_{hp}(x) = \frac{\sigma_{hadr}(x)}{\sigma_{parton}(x)}, \tag{4.10}$$

where $\sigma_{hadr}(x)$ represents the cross section at hadron (particle) level, whereas $\sigma_{parton}(x)$ stands for the cross section calculated at the parton level. Hadron-parton correction $C_{hp}(x)$

is calculated with Pythia. Using only LO generator to calculate the hadron-parton correction and applying it to the NLO parton calculation is inconsistent; however, it is the only possibility to get the theoretical prediction at the hadron level since there is no NLO Monte Carlo particle generator available. If the experimental measurements where presented in certain bins in x, the NLO calculation as well as the hadron-parton correction has to be carried out in the same manner.

4.4 FastNLO

To fit the theoretical prediction to the experimental data requires to redo the calculation many times with different parameter setup. For example, to determine the coupling constant α_s we have to introduce a function $\chi^2(\alpha_s(M_Z))$ to be minimalized which quantifies the similarity between data and theory. This function has to be provided for arbitrary value of $\alpha_s(M_Z)$, demanding that also the theoretical prediction of the observable must be available for any value of $\alpha_s(M_Z)$.

In the majority of cases the NLO computation is extremely slow because there are more jet present in the final state. To speed up the calculation the new interface fastNLO [22] was developed by Thomas Kluge, Klaus Rabbertz and Markus Wobisch. FastNLO is an approach that factorizes out the α_s and the PDF dependence from the hard process matrix element in the cross section. This factorization allows flexible theoretical calculation for any PDF and any $\alpha_s(M_Z)$.

The general formula for the cross section in a hadron-hadron collisions is given by

$$\sigma_{hh}(x_1, x_2) = \sum_n \alpha_s^n(\mu_r) \sum_i^{flavors} \sum_j^{flavors} c_{i,j,n}(x_1, x_2; \mu_r, \mu_f) \otimes f_i(x_1, \mu_f) \otimes f_j(x_2, \mu_f), \quad (4.11)$$

where x_1, x_2 are hadron momentum fractions, carried by partons when entering the hard interaction, $c_{i,j,n}$ are coefficient obtained in perturbation theory at the order of α_s^n, the f_i function denotes the parton i density in the hadron and μ_r, μ_f describe the renormalization, and factorization scales, respectively.

The PDF f_i dependence on factorization scale is dictated by the DGLAP evolution equations $f(x) \overset{DGLAP}{\rightarrow} f(x, \mu_f)$. The key idea of fastNLO is to write the distribution function as a linear combination of polynomial eigenfunctions $E^i(x)$ and expansion coefficients $f(x^i)$

$$f(x) = \sum_i f(x^i) E^i(x), \quad (4.12)$$

calculate the process not for the whole distribution function of hadron, but for the eigen functions $E^i(x)$ in LO and NLO separately and then sum the contributions multiplied by the factors $f(x^i)$.

The x axis is divided into a number of generally overlapping regions, each one denoted by the index i, with a center x^i. There are 10 such x regions in which the PDFs are

expanded in fastNLO. The number of bins was sufficient to approximate the PDFs with the precision of 0.2%. The product of two PDFs $f_k(x)$, $f_l(x)$ is then

$$f(x_1, x_2) = \sum_{i,j} f(x^i, x^j) E^{ij}(x_1, x_2) \equiv \sum_{i,j} f(x^i) f(x^j) E^i(x_1) E^j(x_2) \tag{4.13}$$

There are only seven relevant distinct partonic subprocesses in the hadron-hadron jet production. Denoting gluon, quark and antiquark distribution functions in the proton by $g(x)$, $q_i(x)$, $\bar{q}(x)$, respectively, they are $(i \neq j)$

$$\begin{array}{rcrcl}
 & & gg \to jets & \equiv & H_1(x_1, x_2) \\
qg \to jets & + & \bar{q}g \to jets & \equiv & H_2(x_1, x_2) \\
gq \to jets & + & g\bar{q} \to jets & \equiv & H_3(x_1, x_2) \\
q_i q_j \to jets & + & \bar{q}_i \bar{q}_j \to jets & \equiv & H_4(x_1, x_2) \\
q_i q_i \to jets & + & \bar{q}_i \bar{q}_i \to jets & \equiv & H_5(x_1, x_2) \\
q_i \bar{q}_i \to jets & + & \bar{q}_i q_i \to jets & \equiv & H_6(x_1, x_2) \\
q_i \bar{q}_j \to jets & + & \bar{q}_i q_j \to jets & \equiv & H_7(x_1, x_2)
\end{array}$$

They can be rewritten in terms of functions that are connected to the parton distribution densities

$$\begin{aligned}
G(x) &= g(x), \\
Q(x) &= \sum_i q_i(x), \\
\bar{Q}(x) &= \sum_i \bar{q}_i(x), \\
S(x_1, x_2) &= \sum_i (q_i(x_1) q_i(x_2) + \bar{q}_i(x_1) \bar{q}_i(x_2)), \\
A(x_1, x_2) &= \sum_i (q_i(x_1) \bar{q}_i(x_2) + \bar{q}_i(x_1) q_i(x_2)),
\end{aligned} \tag{4.14}$$

as

$$\begin{aligned}
H_1(x_1, x_2) &= G(x_1) G(x_2), \\
H_2(x_1, x_2) &= (Q(x_1) + \bar{Q}(x_1))\, G(x_2), \\
H_3(x_1, x_2) &= G(x_2)\, (Q(x_2) + \bar{Q}(x_2)), \\
H_4(x_1, x_2) &= Q(x_1) Q(x_2) + \bar{Q}(x_1) \bar{Q}(x_2) - S(x_1, x_2), \\
H_5(x_1, x_2) &= S(x_1, x_2), \\
H_6(x_1, x_2) &= A(x_1, x_2), \\
H_7(x_1, x_2) &= Q(x_1) \bar{Q}(x_2) + \bar{Q}(x_1) Q(x_2) - A(x_1, x_2).
\end{aligned} \tag{4.15}$$

Thus we have narrowed the number of independent distribution functions to be used in the calculation to down seven. The formula for the cross section (4.11) turns into the form

$$\sigma_{hh}(x_1, x_2) = \sum_n \alpha_s^n(\mu_r) \sum_{k=1}^{7} c_{k,n}(x_1, x_2; \mu_r, \mu_f) \otimes H_k(x_1, x_2, \mu_f). \tag{4.16}$$

This is not new, such a simplification is implemented in NLOJET++ also. The crucial point comes writing down the functions H_k in terms of the eigenfunctions $E^{i,j}$. The distribution functions of elementary subprocesses H_k are expressed in terms of the eigenfunction $E^{i,j}$ as

$$H_k(x_1, x_2) = \sum_{i,j} H_k(x^i, x^j) E^{i,j}(x_1, x_2), \tag{4.17}$$

where $H_k(x^i, x^j)$ is a number. Plugging the last relation in the formula for the jet cross section (4.16) we factorize the dependence on α_s and the PDF expansion coefficients H_k

$$\sigma_{hh}(x_1, x_2) = \sum_n \alpha_s^n(\mu_r) \sum_{k=1}^{7} \sum_{i,j} H_k(x^i, x^j) \bar{\sigma}_{k,n}^{i,j}, \tag{4.18}$$

where

$$\bar{\sigma}_{k,n}^{i,j} = c_{k,n}(x_1, x_2; \mu_r, \mu_f) \otimes E^{i,j}(x_1, x_2). \tag{4.19}$$

The coefficients H_k contain the whole information about PDF, whereas in $c_{k,n}$ the properties of the observable (the perturbative coefficients, the jet definition) are included.

Since $\bar{\sigma}_{k,n}^{i,j}$ is α_s and PDF independent it has to be computed only once. This calculation is still very-time consuming and must be performed for any desired choice of factorization scale. fastNLO uses NLOJET++ to calculate these coefficients. However, to get the observable prediction for any PDF or α_s, the computation is very fast because the only thing to perform is the sum (4.18).

Chapter 5

Inclusive Jet Production in $p\bar{p}$

The significant determination of α_s from hadron collider data are from $\bar{b}b$ production cross section [23], from prompt photon production [24], and the inclusive jet production cross section. The last measurement was performed by the CDF collaboration at the Fermilab [4]. In this chapter we aim to perform a similar α_s determination, to investigate theoretical uncertainties of the procedure, and get used to the program interface of NLO QCD calculation.

The measurement used in our analysis was performed by the DØ collaboration during Run I (1992–1996) at the Tevatron, in proton-antiproton collisions with a center of mass energy of $\sqrt{s} = 1800\,\mathrm{GeV}$ [7]. The observed differential cross section $\mathrm{d}\sigma/(\mathrm{d}\eta\mathrm{d}E_T)$ is presented as a function of the jet transverse energy E_T in five pseudorapidity (4.1) jet cuts

$$\begin{aligned} 0.0 \leq &\ \eta\ < 0.5 \\ 0.5 \leq &\ \eta\ < 1.0 \\ 1.0 \leq &\ \eta\ < 1.5 \\ 1.5 \leq &\ \eta\ < 2.0 \\ 2.0 \leq &\ \eta\ < 3.0. \end{aligned}$$

The spectrum spans from 50 to 500 GeV in jet transverse energy and drops down over seven orders of magnitude. Distinct E_T bins may serve as statistically independent measurements of α_s, hence the running of the coupling constant can be tested.

The jet production is understood within perturbative QCD as a scattering of two almost free partons. Produced partons in the final state manifest themselves as detector jets. In the perturbative approach, the LO diagrams for the inclusive jet production have two partons in the initial and the final state, therefore, the LO contribution to the cross section is proportional to α_s^2.

For the analysis of the inclusive jet production we use the fastNLO interface described in the previous chapter which provides the cross section calculated at $2 \to 2$ jet processes in NLO. We use the CTEQ6.1M parton distribution functions. Provided forty PDFs in addition to the central PDF allows us to explore the theoretical uncertainties originating in the imperfect knowledge of the proton/antiproton structure. The theoretical prediction is

calculated in each E_T bin with the same width as in the data in order to directly compare the theoretical prediction with the measurement. The inclusive cross section is depicted in Fig. 5.1. Solid lines represent the theoretical calculation with the choice of $\alpha_s(M_Z) = 0.118$ and the renormalization and factorization scales satisfying $\mu_r = \mu_f = 0.5E_T^{max}$, where E_T^{max} is an energy of the most energetic jet (leading jet) in the single collision event. The calculated theoretical prediction is multiplied by the hadron-parton correction $C_{hp}(E_T)$ in order to obtain appropriate quantity to be compared with the data as discussed in the paragraph before the equation (4.10). The hadronization effects are illustrated in Fig. 5.2.

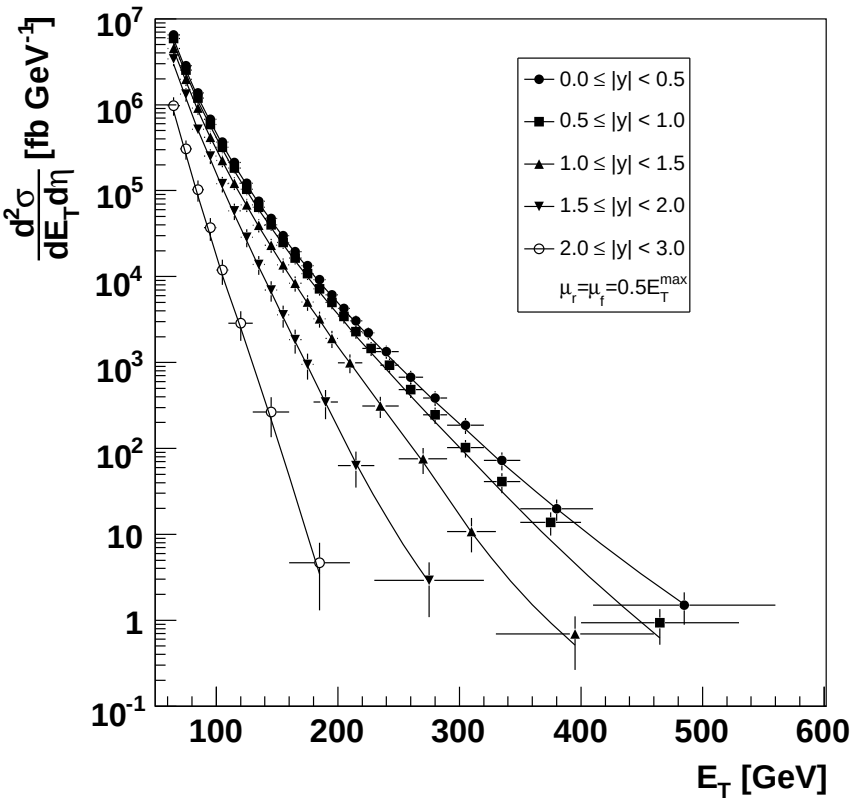

Figure 5.1: The inclusive jet cross section depicted as a function of the transverse energy E_T in five pseudorapidity cuts. The theoretical prediction is calculated with $\alpha_s(M_Z) = 0.118$ and corrected for hadronization.

We see that the hadron-parton correction is about 5% in the central pseudorapidity region $0.0 \leq |\eta| < 0.5$ and increases up to 10% for the last η region. The fact that there is not as many hadronic jets in particular E_T bin can be readily understood. The energy of high energetic partons in the final state will be slightly redistributed in the $\eta \times \phi$ plane due to hadronization. In some cases, for example with two parton jets in the final state, the event will evolve into three particle jets after the hadronization, or generally into more than two

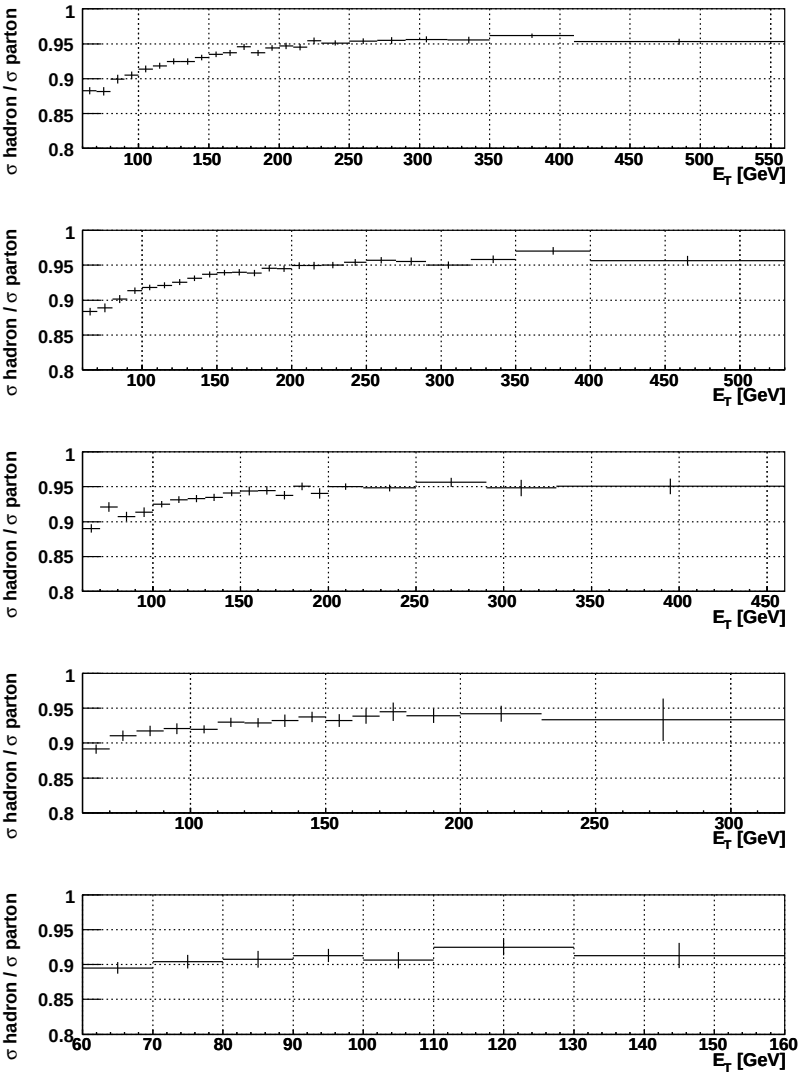

Figure 5.2: Hadron-parton correction for the inclusive jet cross section given in five pseudorapidity cuts from top to bottom: $|\eta| < 0.5, 1.0$, 1.5, 2.0, 3.0. It is about 5% to 10% for the p_T values over 200 GeV.

hadron jets. Every created particle jet will carry less momenta than the original parton jet, and therefore it will not contribute to the same E_T bin as the parton jet. Since the cross section is a steeply falling distribution as a function of E_T this results in a lack of hadron jets in all E_T bins.

The use of jet algorithm has an extra subtlety for the Run I measurements. We have stated, that this algorithm is not infrared safe. Additional radiation of soft parton might spoil the behavior of the jet observable. It cannot be used on the theory side, the theoretical calculation must be done with some IR safe jet algorithm. In fastNLO, the cross section was calculated with the Run II midpoint algorithm because it is better behaved in the calculation at the parton level. However, the comparison of observables obtained with different algorithms is inconsistent. One should also study the influence of the algorithm correction C_{alg} on the predicted cross section σ^{data} to be compared with the real measurement

$$\sigma^{data} = C_{alg} C_{hp} \sigma^{NLO}_{midp}, \quad C_{alg} = \frac{\sigma^{hadr}_{Run\ I}}{\sigma^{hadr}_{midp}}, \quad C_{hp} = \frac{\sigma^{hadr}_{midp}}{\sigma^{part}_{midp}}. \tag{5.1}$$

C_{hp} denotes the previously discussed hadron-parton correction (4.10) calculated in Pythia with the IR safe midpoint Run II cone algorithm, $\sigma^{hadr}_{Run\ I}$ and σ^{hadr}_{midp} are the inclusive cross section on the hadron level calculated with the Run I algorithm and the Run II algorithm, respectively.

For the inclusive cross section the situation is though very simple. The algorithm correction was studied and found to be less then 0.1% in all pseudorapidity regions, hence negligible. $C_{alg} = 1$ can be considered.

5.1 Discussion of Uncertainties

It is crucial to treat all theoretical and experimental uncertainties to determine the error on $\alpha_s(M_Z)$. We may estimate on the approximate basis how will an uncertainty of the inclusive cross section due to various effects will propagate to uncertainty on $\alpha_s(M_Z)$. As we stated above, the LO contribution to the S-matrix is proportional to α_s^2. A small change in $\alpha_s(M_Z)$ for example by 10% has a 20% impact on the observable. And vice versa, knowing the uncertainty on jet cross section, we may expect better precision on $\alpha_s(M_Z)$ by a factor of two.

The experimental uncertainty is dominated by the systematic uncertainty due to the calibration of the jet energy (JES – jet energy scale). In the case of the inclusive jet cross section, this systematic uncertainty ranges from about 12% to 20% at low E_T and increases up to 80% at high E_T.

There are two major theoretical uncertainties. The first comes from the dependence of inclusive cross section on the parton distribution functions which were extracted from different experiments. The second uncertainty is due to the renormalization and factorization scale choice. Even though the value can be picked arbitrary because it diminish from the calculation at the infinite order, the finite order perturbative expansion of the cross section depends on this scale. There has been several proposals to fix the renormalization

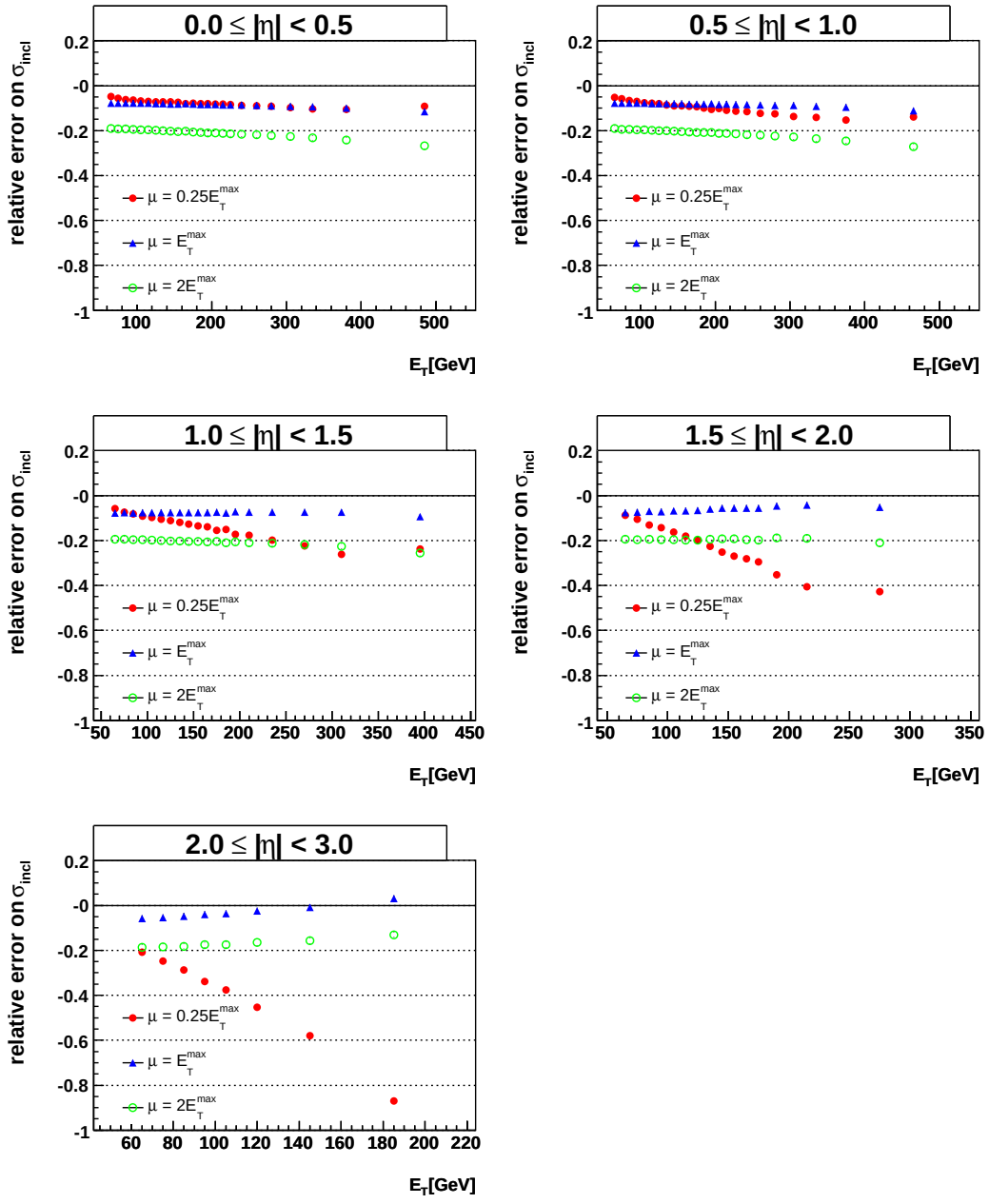

Figure 5.3: Renormalization dependence of the inclusive jet production. It is computed for three scales $\mu_r = \mu_f = 0.25, 1.0, 2.0\, E_T^{max}$ and compared to the scale $\mu_r = \mu_f = 0.5 E_T^{max}$.

scale in finite order of perturbation theory – e.g Principal of minimal sensitivity (PMS) [26], effective charge method [27], or Brodsky, Lepage and Mackenzie (BLM) method [28]. Here, we do not precisely explore the overall scale dependence to find for example the point where the cross section is weakly scale dependent (PMS), but choose the central scale $\mu_r = 0.5\,E_T^{max}$ and study the cross section behavior around this value, for scales $0.25E_T^{max}$, $1E_T^{max}$, $2E_T^{max}$. The factorization and renormalization scales were set equal $\mu_r = \mu_f$ and varied together. Again, E_T^{max} denotes the most energetic jet in the event. The choice of the central scale $0.5\,E_T^{max}$ corresponds roughly to a maximum of the cross section as a function of the scale μ_r as is depicted in Fig. 5.3 where all the scale variation give values lower than the central scale $\mu_r = 0.5\,E_T^{max}$. The scale uncertainty is about 20% in the first three pseudorapidity regions which is a value comparable to the experimental systematic uncertainty but the effect of the scale change can rise up to 100% for forward jets $1.5 \leq |\eta| < 2.0$ and $2.0 \leq |\eta| < 3.0$.

To study the PDF dependence of the observable, we use forty PDFs in CTEQ6.1M and determine the uncertainty on the cross section according to the formula (3.27). The obtained relative error is displayed in Fig. 5.4. Low E_T bins are affected with the uncertainty approximately of 5% only, but the uncertainty increases up to 40% for the $E_T = 500\,\mathrm{GeV}$. In this domain, the large error originates from the uncertainty on the gluon density. The gluon momentum density falls as a function of the proton momentum fraction carried by gluon, which can be for central jets expressed as

$$x \sim \frac{2E_T}{\sqrt{s}}. \tag{5.2}$$

This behavior is seen in the top of Fig. 5.5. The gluon PDF uncertainty rises significantly as one approaches the domain of transverse jets with $x \sim 10^{-1}$, see the bottom of Fig. 5.5.

5.2 Determination of α_s

As we mention earlier, different E_T bins can be used to extract the coupling constant α_s and to show its evolution as a function of transverse momentum. To accomplish this goal we have to fit the data to the theoretical calculation corrected for the hadronization effects.

Generally, the prediction of the theory has three free parameters: the strong coupling defined at the scale M_Z, the renormalization scale μ_r, and the factorization scale μ_f. Only the coupling will be considered as a free parameter. The scales will be set to fixed values $\mu_r = \mu_f = 0.5\,E_T^{max}$, but in addition we estimate the impact of the particular scale choice on $\alpha_s(M_Z)$. The χ^2 function that has to be minimalized is defined as

$$\chi^2 = \left[\frac{D - T(\alpha_s(M_z), \mu_r, \mu_f)}{\sigma}\right]^2, \tag{5.3}$$

where T, and D denotes theoretical prediction, and experimental measurement respectively, and σ is the total experimental uncertainty, statistical and systematic uncertainty

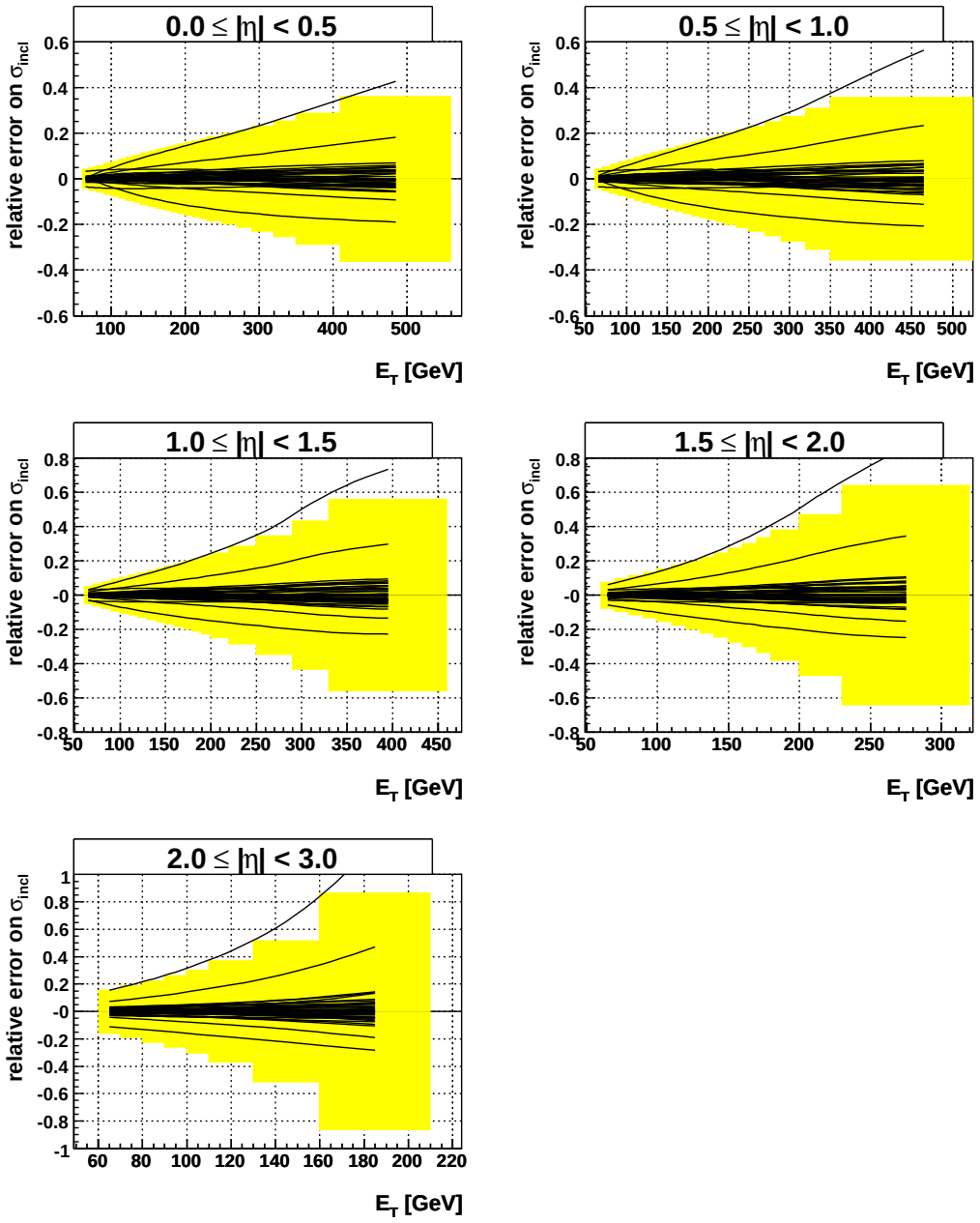

Figure 5.4: The relative uncertainty due to the choice of PDF on the inclusive E_T spectrum. The solid lines represent the calculation for different PDF sets in CTEQ6.1M. The shaded region corresponds to the error on the cross section calculated with formula (3.27).

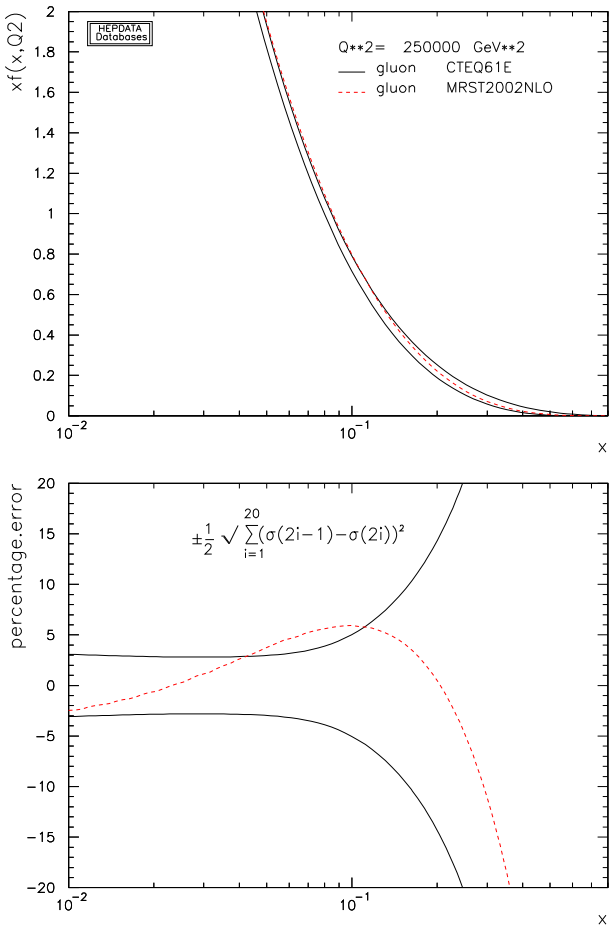

Figure 5.5: The gluon momentum density inside the proton (top) and the uncertainties of this distribution in CTEQ61E and MRST2002NLO (bottom). The figures were calculated with the on-line PDF calculator [29].

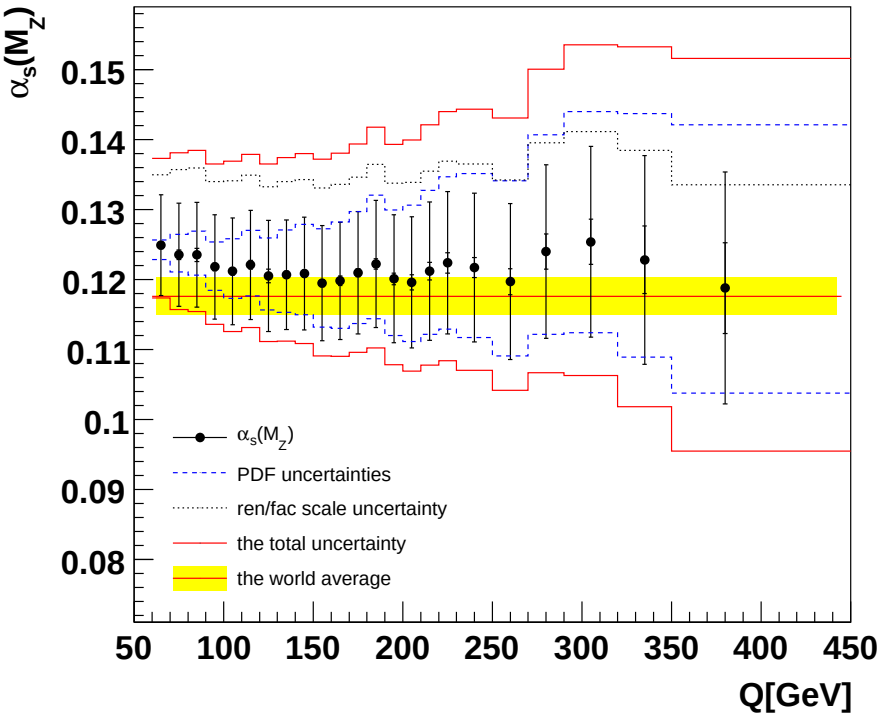

Figure 5.6: The fit of $\alpha_s(M_Z)$ in every E_T bin in the region $0.0 < \eta \leq 0.5$.

add in quadrature. This function is minimized for every E_T bin in the central pseudorapidity region $0.0 < \eta \leq 0.5$ and thus the value $\alpha_s(M_Z)$ is obtained independently for any momentum bin. Only the first pseudorapidity region is considered here, since we plan to compare our theoretical estimates with the CDF measurement which was performed for jets located in the central calorimeter. The fit results are depicted in Fig. 5.6. The extracted values are slightly above the world average $\alpha_s(M_Z) = 0.1182 \pm 0.0027$ which is illustrated by the straight line.

The uncertainty on $\alpha_s(M_Z)$ was obtained in three steps. First, we obtain the experimental uncertainties from the fit. The experimental systematic uncertainty is visualized with the large error bars in Fig. 5.6. The smaller error bars correspond to the statistical uncertainties. Secondly, the uncertainty which has the greatest impact on the measured $\alpha_s(M_Z)$ originates in the inaccuracy of PDFs which spans from 2% for low E_T bins to 16% for 400 GeV bins. They have been attained by fitting the shifted theory in two directions along the PDF uncertainty, seen in Fig. 5.4 as a shaded region. We see that this uncertainty, marked with the dashed line in Fig. 5.6, is comparable with the experimental

uncertainties. Lastly, we have to consider the choice of a scale. The Fig. 5.3 reveals that the choice $\mu_r = \mu_f = 0.5E_T^{max}$ corresponds to the local maximum in cross section as a function of the scale. To establish the uncertainty, we vary the scale along the central value by a factor of 2, $\mu_r = \mu_f = 0.25E_T^{max}$, $\mu_r = \mu_f = E_T^{max}$. The scale change in any direction leads to the decrease of the cross section. Hence there is an asymmetric uncertainty in $\alpha_s(M_Z)$ due to the renormalization scale illustrated by the dotted line.

Instead of fitting α_s at fixed scale we can directly obtain α_s at the scale of the process Q calculated as a center of a particular E_T bin. The final result of strong coupling constant evolution is seen in Fig. 5.7. We distinguish between the experimental statistical uncertainties delineated by the marker error bars and experimental systematic uncertainties sketched underneath the diagram, and expressed in per cents. The region which spreads between the dashed lines corresponds to the total uncertainty (statistical and systematic experimental uncertainties, plus scale and PDF uncertainties add in quadrature).

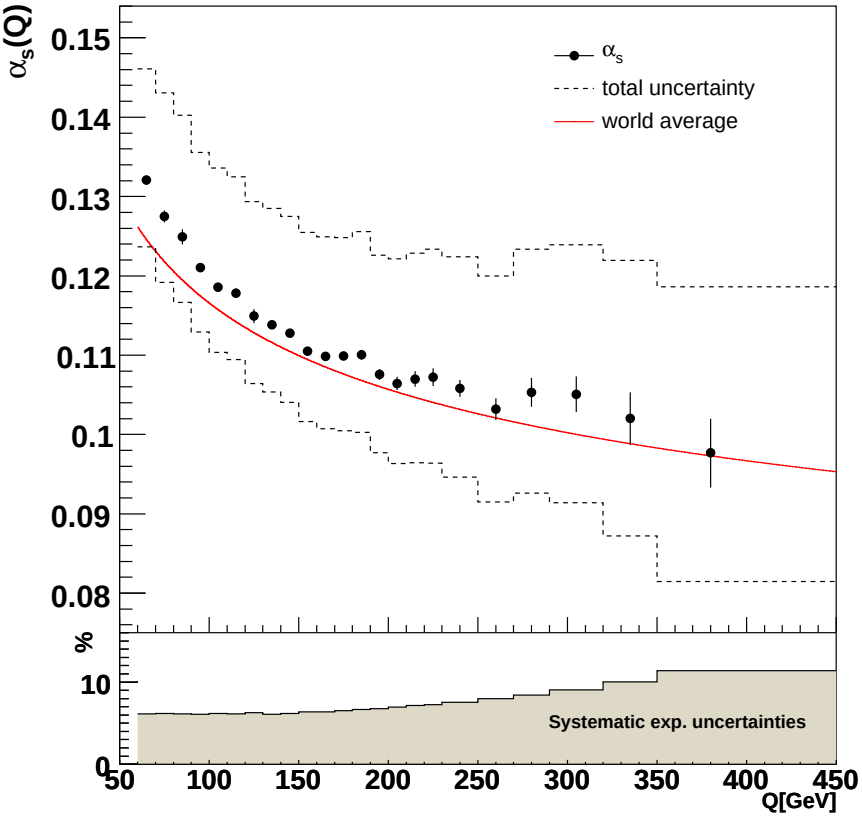

Figure 5.7: Running of α_s. The solid line represents running of α_s calculated from the world average value $\alpha_s(M_Z) = 0.1176 \pm 0.0020$.

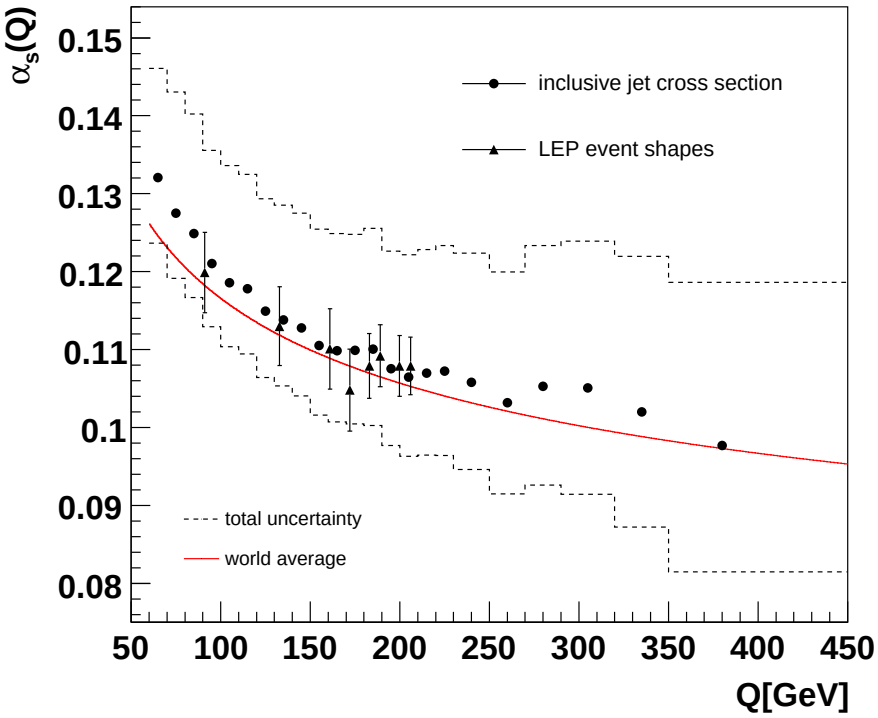

Figure 5.8: Running of the coupling constant compared with the LEP jet shape measurement. The solid line represents the evolution of α_s according to the world average.

5.3 $\alpha_s(M_Z)$ Measurement

So far, we have studied the strong coupling running, fitting the theory to the data in distinct E_T bins. However we may include the information from all the bins and determine a single value of $\alpha_s(M_Z)$. We will take into account the nontrivial correlation between different data bins which were also provided in the article [7] in the form of a correlation matrix C_{ij}. The χ^2 function was defined as

$$\chi^2 = \sum_{i,j} \delta_i H_{ij} \delta_j, \quad \delta_i = T_i - D_i \tag{5.4}$$

different bins being indexed by i, j, where the Hessian matrix H_{ij} is the inverse matrix according to

$$H_{ij} = \left[\frac{T_i}{D_i} C_{ij} \frac{T_j}{D_j} \right]^{-1}. \tag{5.5}$$

Such a χ^2 definition was introduced to resolve the problem of cross section normalization. Many of the systematic uncertainties affecting the normalization are partially or fully correlated across E_T and η. The standard χ^2 definition would prefer theoretical prediction that have a normalization below that of the data. It has been demonstrated that a modified definition of χ^2 is needed to remove this bias [30].

However the procedure of fitting is relatively straightforward we experienced the following difficulties. The presented χ^2 definition (5.4) calculated with the published correlation matrix favors high values of $\alpha_s(M_Z)$. The deeper study of terms contributing to the χ^2 revealed unreasonably very strong correlation between the first three bins of the measurement for $|\eta| < 0.5$. Removing them from the fit we obtain

$$\alpha_s(M_Z) = 0.1227 \pm 0.0071. \tag{5.6}$$

However, since the behavior of the χ^2 with the correlation included could not be understood, we use the systematic uncertainty from the last equation as some higher estimate of the systematic uncertainty and do not use correlations in the following study of theoretical uncertainties of $\alpha_s(M_Z)$.

Performing the fit for the cross section evaluated at different scales ($\mu_r = \mu_f = 0.25E_T^{max}, 1E_T^{max}$) and including the PDF uncertainty illustrated as a shaded region in Fig. 5.4 we arrive with the final result of the strong coupling

$$\alpha_s(M_Z) = 0.1212 \pm 0.0001(stat.) \pm 0.0070(syst.)^{+0.0094}_{-0.0074}(PDF)^{+0.0053}_{-0}(scale). \tag{5.7}$$

The value of systematic uncertainty 6 % coincides with our previously estimated error; it is roughly half of the cross section systematic uncertainty. The PDF theoretical uncertainty is $6-7$ %, and is comparable with the experimental uncertainty. Last, the scale uncertainty $\alpha_s(M_Z)$ is only in one direction and is approximately 4%.

5.4 Comparison with CDF and LEP

Let us now compare the above results with other measurements which were dedicated to the α_s determination. First to mention is the CDF paper [4]. It analyzes the measurement of inclusive jet production over the transverse energy E_T range from 40 to 450 GeV, with η in $0.1 < |\eta| < 0.7$. The presented value of measured strong coupling is

$$\alpha_s(M_Z) = 0.1178 \pm 0.0001(stat.)^{+0.0081}_{-0.0095}(exp.syst.), \tag{5.8}$$

where the two uncertainties denote the experimental statistical and systematic errors. Published theoretical uncertainty associated with the choice of PDF is approximately 5%. There was no systematic PDF uncertainty study similar to that in CTEQ6.1M present at the time of CDF publication. The only way to evaluate the PDF uncertainty was to compare predictions obtained with other known distribution functions, more specifically with PDFs called MRST provided by the Durhem PDF group. The particular choice of renormalization scale $\mu = E_T^{max}$ produces uncertainty $^{6\%}_{4\%}$. We see that the CDF theoretical

uncertainties are comparable with our result. The final CDF result of $\alpha_s(M_Z)$ is compatible with our calculation within errors. It should be noted, that the CDF results are not corrected for hadronization effects, which could possibly higher the value of $\alpha_s(M_Z)$.

One of the most exact determination of α_s comes from the LEP measurement. We compare our result with event shapes study at LEP [3]

$$\alpha_s(M_Z) = 0.1202 \pm 0.0003(stat.) \pm 0.0049(total.syst.). \tag{5.9}$$

The discussion of theoretical uncertainties for this measurement was published and can be found in [31]. LEP measurement has the largest uncertainty due to the theoretical calculation ($\sim 4\%$). The measurement itself is very precise, the experimental uncertainty on $\alpha_s(M_Z)$ is only $\sim 1\%$ in comparison to the DØ, measurement which suffers from the experimental uncertainty $\sim 6\%$. LEP and DØ results of the α_s running are summarized in Fig. 5.8. Both measurements of α_s are presented with the total uncertainties.

The electron positron scattering allows to achieve roughly twice as better precision on $\alpha_s(M_Z)$ than that from proton antiproton collisions. There are at least two reasons for this, due to the fact that no hadrons are present in the initial state in the LEP measurement. First, in hadron-hadron scattering we do not know the invariant mass of the initial state partons to be involved in the hard interaction. The initial state partons carry the hadron transverse momentum fraction x, which varies from event to event. In case of LEP, the center of mass energy is known (except for the case when a photon is emitted from the inital state electron, but the data can be corrected on this effect) and it provides an additional information about the jet energy scale calibration and the jet reconstruction. Moreover, LEP events are much cleaner. There are no beam remnants travelling in the direction of the beam to interact with produced, transversally outgoing partons. Secondly, there is no additional uncertainty due to the parton distribution functions in $e^+\,e^-$ annihilation in the theoretical calculation.

The asymptotic freedom predicts a logarithmic decrease of the strong coupling strength $\alpha_s(\mu)$, as the momentum scale μ characterizing a process increases. Determination of the strong coupling is a fundamental measurement and the observation of running of the coupling constant is one of the key test of the theory. We have attained to determine this running from the inclusive jet production cross section which is compatible with the two-loop approximation of the α_s evolution (3.20). This is visualized in the Fig. 5.7 and 5.8.

Even though we were unable to extract $\alpha_s(M_Z)$ using all of the information published in the article due to the systematic correlations, we could estimate the theoretical uncertainties coming from PDF and the renormalization scale which turned compatible with the analogous CDF analysis. Having gained enough experience with the analysis of the inclusive jet production cross section, we will turn to study another DØ measurement.

Chapter 6

Dijet Azimuthal Decorrelation Spectrum in $p\bar{p}$

In the previous chapter, we studied the inclusive jet production and determined the strong coupling constant. The jet cross section depends directly on the transverse momentum of the jet and is thus very much influenced by the uncertainty on the jet energy calibration (JES) which had the most significant role between all the experimental uncertainties. On the theory side, the greatest contribution to the calculated cross section originated from PDFs. The interesting question is whether there exist other observables which are less sensitive to the JES calibration and to PDFs, and thus allow us to measure the coupling constant with a higher precision. Namely, the question is whether we can benefit from the newly developed tool and perform α_s measurement from some more suitable 3-jet observable. Several such observables were measured by the DØ collaboration but only few were corrected for the effects due to the finite detector resolution. Only such measurements can be considered for a consistent α_s analysis.

We chose the measurement of dijet azimuthal decorrelation spectrum for our analysis and we will see that it has the desired properties for determination of α_s. The observable was defined as the ratio

$$\frac{1}{\sigma_{dijet}}\frac{\mathrm{d}\sigma_{dijet}}{\mathrm{d}\Delta\phi}, \tag{6.1}$$

of a differential cross section depending on the azimuthal angle $\Delta\phi = |\phi_{jet1} - \phi_{jet2}|$ between the two leading jets, i.e. jets with the highest transversed momenta, normalized to the total cross section. The azimuthal angle is an angle between two jets projected onto the plane perpendicular to the beam. The angle between jets is outlined in the Fig. 6.1. Smaller angle between the leading jets is the consequence of additional hard jet radiation. The crucial property is that the $\Delta\phi$ distribution is defined as a ratio of the differential and the total cross section Therefore, the systematic uncertainties cancel and the JES dependence of the spectrum is reduced. As we will see more explicitly, another direct consequence of the definition as the ratio is that the contribution from PDF cancels also. Consequently, the theoretical uncertainty on $\Delta\phi$ spectrum due to PDF is lowered.

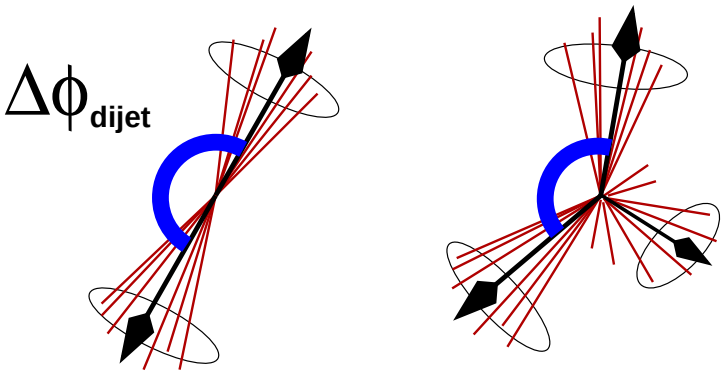

Figure 6.1: The angle $\Delta\phi$ between two jets with the highest transverse momentum. The angle decreases as more jets are observed.

The analysis given in this section is based on the published measurement of dijet azimuthal decorrelation spectrum [6] in $\bar{p}p$ collisions performed by DØ collaboration at the Tevatron during the so called Run II. A center of mass energy of colliding hadrons was extended to $\sqrt{s} = 1960\,\text{GeV}$ from the Run I.

The measurement was carried out in four separate transverse momentum p_T^{max} regions where p_T^{max} represents the momentum of the leading jet in the event: $p_T^{max} > 75, 100, 130, 180\,\text{GeV}$. The second jet in the event was required to have the momentum at least $p_T > 40\,\text{GeV}$ and both of the most energetic jets had to be located in the central region of the calorimeter, with the true rapidity (4.4) in the range $|y_{jet}| < 0.5$.

The measured distribution is seen in Fig. 6.2. It is a steeply rising function of $\Delta\phi$, with the maximum at π. The peak corresponds to the kinematic setup when two leading jets are perfectly back-to-back, forming the straight angle.

Along data markers, a theoretical prediction calculated with NLOJET++ is presented. It is evaluated for the value of $\alpha_s(M_Z) = 0.118$ and with the use of CTEQ6.1M (central value) parton distribution function. The theoretical definition of the angular decorrelation spectrum is the ratio of differential cross section $2 \to 3$ jet processes $\mathrm{d}\sigma_{dijet}/\mathrm{d}\Delta\phi$, and the total $2 \to 2$ jet cross section σ_{dijet}, both calculated at LO, or NLO:

$$\text{observable } \mathscr{O} = \frac{1}{\sigma_{dijet}}\bigg|_{(N)LO} \frac{\mathrm{d}\sigma_{dijet}}{\mathrm{d}\Delta\phi}\bigg|_{(N)LO}. \tag{6.2}$$

The LO curve vanishes for values $\Delta\phi < \frac{2}{3}\pi$ which is due to the fact that there are at most three jets produced in the $2 \to 3$ jet LO calculation. A conservation of momentum demands the overall transverse momentum to be balanced hence; the two leading jets cannot form an angle smaller then $2/3\pi$. In this special configuration, we find three jets in the final state, all with equal transverse momenta. In NLO however, we have an additional jet present in the final state which makes it possible to receive contributions at smaller

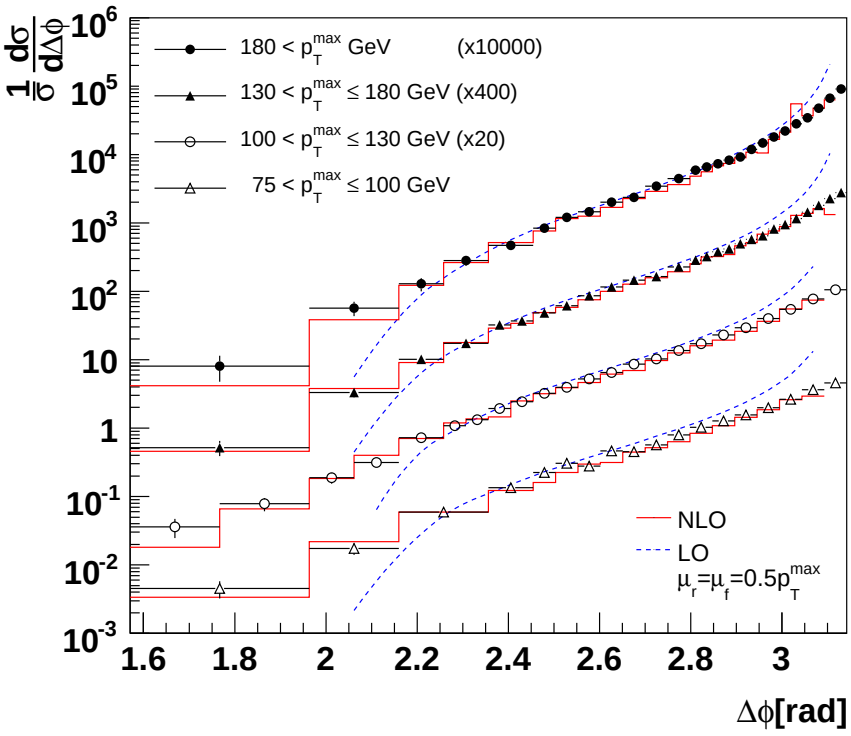

Figure 6.2: The dijet azimuthal decorrelation spectrum shown in four p_T^{max} bins. Theoretical prediction was calculated in LO and NLO using $\alpha_s(M_Z) = 0.118$.

angles. The evaluation of $2 \to 3$ jet NLO processes is essential to properly describe the measured spectrum at low $\Delta\phi$.

The theory fails to describe data for values of $\Delta\phi \approx \pi$ since the multi-parton radiation is dominant in this region. One would have to resum higher order contributions of a perturbation series to obtain a satisfactory description of the data. In LO, the differential cross section diverges to $+\infty$ when approaching the edge $\Delta\phi$ interval due to the parton collinear radiation. On the other hand, the distribution falls to $-\infty$ for $\Delta\phi \to \pi$ when the vertex loop Feynman diagrams are included in NLO. Such a resummation at the edge of the phase space is not included in NLOJET++ but is implemented for example in Pythia.

From the Tab. 4.1, outlining the dependence of certain LO (NLO) processes on α_s, we see that the normalized $\Delta\phi$ distribution (6.2) is proportional to the coupling constant:

$$a)\ \text{LO}: \quad \mathscr{O}\big|_{LO} = c_1\alpha_s + \mathcal{O}(\alpha_s^2) \qquad b)\ \text{NLO}: \quad \mathscr{O}\big|_{NLO} = c_1\alpha_s + c_2\alpha_s^2 + \mathcal{O}(\alpha_s^3). \tag{6.3}$$

The LO expansion coefficient c_1 comes from the evaluation of tree-level Feynman diagrams which do not contain loops. Consequently, it is not a function of the renormalization

scale. The higher order perturbative expansion coefficient c_2 receives the non-trivial scale dependence. Anyway, we see that the observable is directly sensitive to α_s and may serve for the determination of the strong coupling constant.

In Chapter 4, we demanded the knowledge of hadron-parton correction of a measured observable in order to compare the data and theory in a systematic way. For the dijet decorrelation which is defined as a ratio, however, this correction is negligible [6], the data and theory can be compared directly.

6.1 Theoretical Uncertainties

A theoretical calculation of a jet observable is not exact; it suffers from uncertainties due to the parton distribution functions used in the calculation and the renormalization plus the factorization scale choice. We will now discuss their effects on the $\Delta\phi$ distribution.

The PDF dependence was studied using the CTEQ6.1M set which contains forty additional distribution functions devoted to the uncertainty studies. The theoretical prediction for any member of the set compared to the distribution function of the best fit is seen in Fig. 6.3. The calculations were performed with NLOJET++ for $\alpha_s(M_Z) = 0.118$. The uncertainty is calculated according to the formula (3.27) and the result corresponds to the shaded region in the last mentioned figure. The prediction was carried out in LO only where the calculation is relatively fast, keeping in mind, that the effect of the NLO to the PDF ratio is suppressed approximately by a factor of ten. The uncertainty is roughly half of the PDF uncertainty on the inclusive jet cross section where the PDF directly enters the hadron cross section (3.24). Thus we have verified our prediction that the observable defined as a ratio of two cross sections will suffer less from the PDF uncertainty.

The indirect dependence of the $\Delta\phi$ distribution on the PDF can be deduced from the shape of the PDF uncertainty. The function which gives the largest rational error is, as in the case of the inclusive jet cross section, the gluon PDF [32]. It decreases as a function of $\Delta\phi$ in all p_T^{max} regions which is due to the fact that the gluon and quark radiation is different. The gluon radiates additional jet more often than the quark hence it yields larger contribution at low $\Delta\phi$ bins. A change in the gluon distribution function implies the corresponding distribution modification at low $\Delta\phi$.

There is an interesting property in the PDF uncertainty dependence as a function of the transverse momentum p_T^{max}. In the case of inclusive jet production, we saw that the uncertainty grew as E_T increased, Fig. 5.4. For the $\Delta\phi$ spectrum, however, the tendency is reversed. Reaching higher values of p_T^{max}, makes the observable less sensitive to the change of PDF. This property promises that in future colliders where hadrons will be collided with much higher center of mass energy, the evolution of coupling constant could be possible to test more precisely.

Let us now turn to examine the scale dependence. The scale variations were calculated for the particular scales $\mu_r = \mu_f = 0.25p_T^{max}$, $1p_T^{max}$, $2p_T^{max}$ and for $\alpha_s(M_Z) = 0.118$. The difference from the central scale $\mu_r = \mu_f = 0.5p_T^{max}$ is seen in Fig. 6.4. The scale dependence is very strong for $\Delta\phi < 2.3$ rad, in the region where there is the NLO contribution

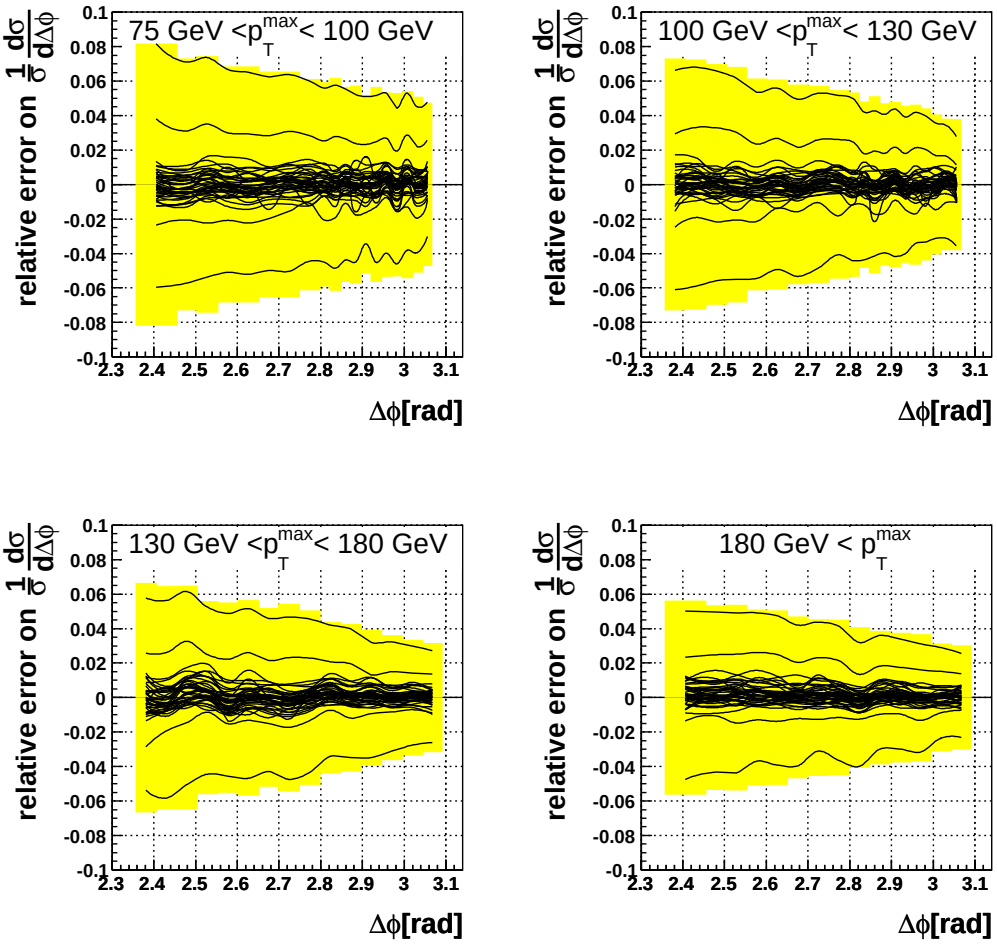

Figure 6.3: The $\Delta\phi$ distribution for the set of forty PDFs CTEQ6.1M. Solid lines represent the prediction for particular PDF, where the shaded region is the uncertainty calculated according to formula (3.27). The greatest contribution to the uncertainty is coming from the gluon PDFs 29, 30 which are at the minimum and maximum of the diagrams, respectively.

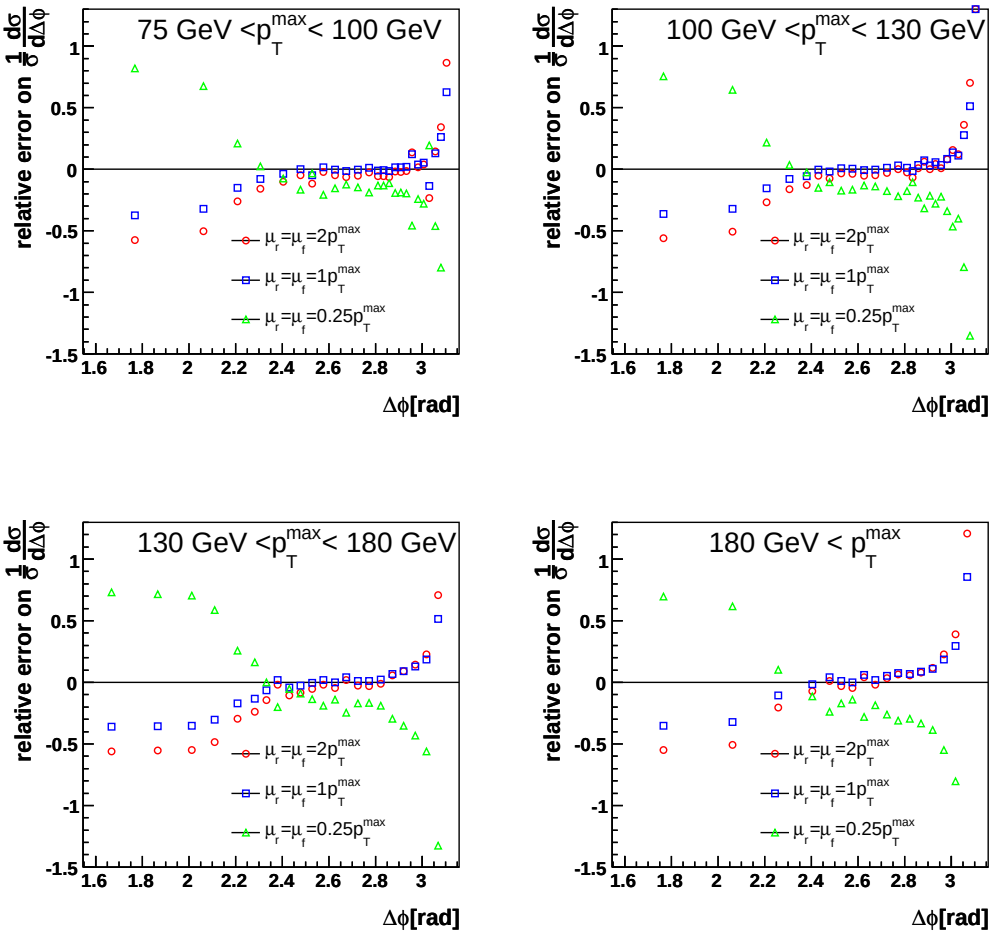

Figure 6.4: The renormalization and factorization scale uncertainty on the $\Delta\phi$ distribution. The central value corresponds to the scale $\mu_r = \mu_f = 0.5\,\mathrm{p}_T^{max}$.

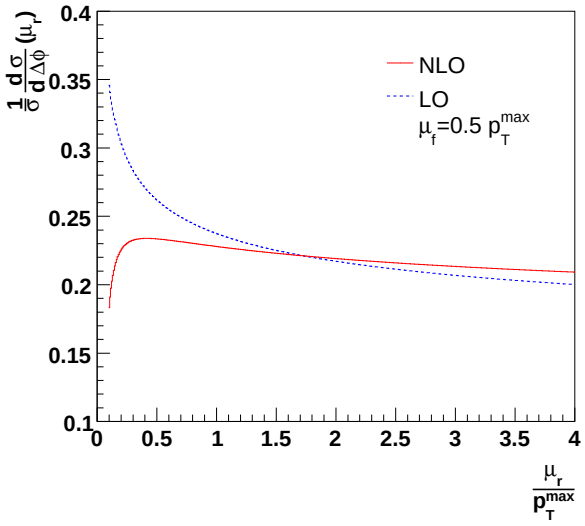

Figure 6.5: The renormalization dependence of the $\Delta\phi$ distribution for $\Delta\phi = 2.6$ rad. The renormalization dependence of the NLO calculation is smaller in comparison to LO.

only. Note that varying the scale for $2.4 < \Delta\phi < 2.8$ rad brings only a small change in the spectrum. This interval is thus suitable for the theory and data comparison because the particular choice of the renormalization and factorization scale does not introduce a very large uncertainty.

The dependence of $\Delta\phi$ spectrum as a function of the renormalization scale only is shown in Fig. 6.5. Advancing to NLO weakens the scale influence. The distribution is relatively flat around the value of $\mu_r = 1p_T^{max}$ which is close to the global maximum. We follow the idea of the Principle of minimal sensitivity [26] suggesting to choose a particular scale in the domain, where the calculation is the least sensitive to the scale change. One then hopes that higher order contributions from the perturbation series will not spoil the weak scale dependence which has been established in LO and NLO. From bin to bin, the renormalization maximum is slightly shifted. Choosing $\mu \equiv \mu_r = \mu_f = 1p_T^{max}$ we can expect approximately symmetrical error on α_s.

6.2 $\alpha_s(M_z)$ Determination

If the coupling constant is to be determined, it is necessary to know how the dijet decorrelation spectrum evolves as a function of $\alpha_s(M_z)$. We used fastNLO interface that gave us the possibility to vary this value arbitrary in the case of the inclusive jet production. There was no such an interface available at the the beginning of our work. We had to develop an alternative approach to fit the theoretical prediction to the data. However, connecting later with one of the authors of fastNLO we could calculated the fastNLO tables for the

dijet decorrelation spectrum. Even though we have eventually used fastNLO to fit the α_s instead of our framework, let us describe in brief the procedure that we followed, to work without the fastNLO interface. It is a general approach that must be applied when one wants to extract $\alpha_s(M_Z)$.

The NLO prediction of three jet observable is very time consuming. It takes about 1000 hours of CPU time to obtain result with a satisfactory statistical precision for evaluating the coupling constant. Our strategy was to calculate the theoretical prediction for five different values of $\alpha_s(M_Z)$ and approximate the $\alpha_s(M_Z)$ dependence of the spectrum in every separate bin by a simple analytic function. Such an approximation is necessary to evaluate χ^2 in the interesting region around the expected value of $\alpha_s(M_Z)$. The data are described with the specific choice $\alpha_s(M_z) = 0.118$ finely in Fig. 6.2, hence we picked five distinct values, $\alpha_s(M_z) = 0.110, 0.120, 0.130, 0.140, 0.150$ in particular, for which to calculate the spectrum.

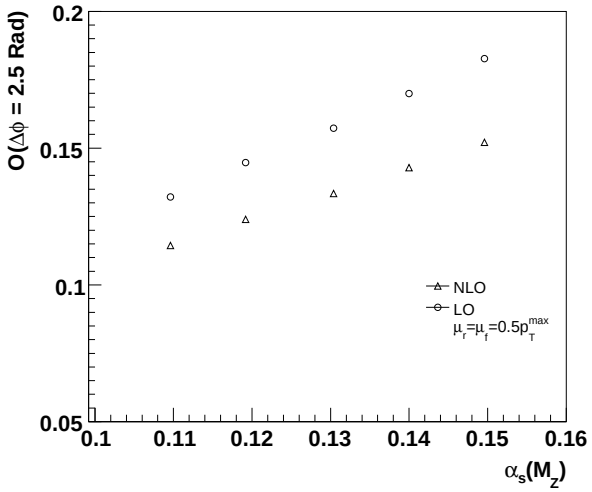

Figure 6.6: The dijet angular spectrum dependence as a function of α_s for $\Delta\phi = 2.5$ rad and the transverse momentum p_T^{max} region $100\,\mathrm{GeV} < p_T^{max} < 130\,\mathrm{GeV}$. The difference between LO and NLO prediction is about 20%.

We mentioned that the $\Delta\phi$ spectrum behaves as a function of α_s accordingly to the equation (6.3). This is illustrated in Fig. 6.6 for LO and NLO calculation. Generally, the NLO contribution to the $\Delta\phi$ distribution is suppressed by a factor of α_s. In the p_T^{max} region $100\,\mathrm{GeV} < p_T^{max} < 130\,\mathrm{GeV}$ this suppression is approximately by a factor of ten. The evolution on α_s was separately fitted in each of 94 bins with the quadratic function (6.3b) thus obtaining the set of 94x2 parameters which approximated the full $\alpha_s(M_Z)$ dependence.

We switched to fastNLO approach mainly because we could obtain much higher statis-

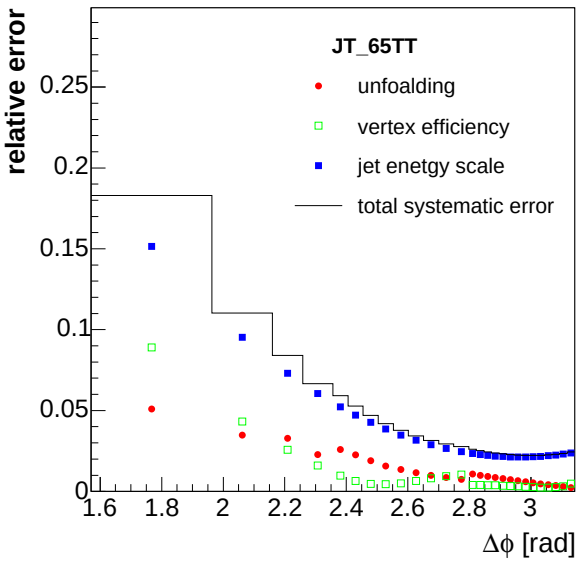

Figure 6.7: Various sources of systematics on the $\Delta\phi$ distribution. The JES has the largest contribution, from [33].

tical precision for any choice of α_s. The very long computation which we performed once with fastNLO would have to be redone five times without it.

To fit the theoretical prediction to the data we have to provide χ^2 function to be minimalized, adjusting the parameter $\alpha_s(M_Z)$. Data are published with the statistical σ^{stat} and the systematic σ^{syst} errors for each data bin, but no information about inter-bin correlation was provided. Although the normalization of the measured spectrum by the total cross section reduces a sensitivity to the jet energy calibration, the calibration still has the greatest impact on the relative systematic uncertainty. The JES contribution to the total experimental uncertainty is depicted in the Fig. 6.7.

The study of JES influence on the $\Delta\phi$ distribution revealed that, in fact, the majority of the data bins in the considered region $2.4 < \Delta\phi < 2.8$ rad are correlated [33]. A change in the JES of about one standard deviation induces the similar shift in all data bins as is illustrated in Fig. 6.7. Therefor, we assume the maximal correlation between data points and construct a correlation matrix C_{ij} in the way that

$$C_{ij} = \left[(\sigma_i^{stat})^2 + (\sigma_i^{syst})^2\right]\delta_{ij} + \sigma_i^{syst}\sigma_j^{syst}, \tag{6.4}$$

where δ_{ij} denotes the Kronecker symbol. It is 1 if $i = j$ and 0 otherwise. The χ^2 is then defined as

$$\chi^2 = \sum_{i,j} \delta_i H_{ij} \delta_j, \quad \delta_i = T_i - D_i, \tag{6.5}$$

where H denotes the Hessian matrix calculated as an inverse of the covariant matrix $H = C^{-1}$, and T_i, D_i are theory and data bins, respectively. The indices i, j run over

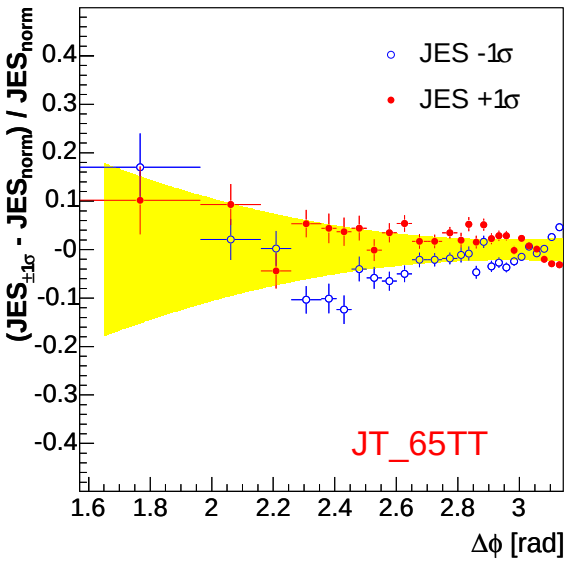

Figure 6.8: Relative change of $\Delta\phi$ distribution derived using the upper (full circles) and the lower (open circles) error value of jet energy scale with respect to the nominal value of JES. The shaded region is smooth and symmetrized difference that is used as an estimate of the systematics connected with the error on JES, from [33].

32 data points included in the fit. They are in the range $2.4 < \phi < 2.8$ rad where the renormalization uncertainty tends to be the smallest.

As in the last chapter, the uncertainties of $\alpha_s(M_Z)$ where obtained in three steps, determining the experimental uncertainties, an uncertainty due to the PDF and an error due to the scale choice. The data points included in the fit has the systematic uncertainty ranging roughly from 3% to 8% (an example Fig. 6.7). We included the maximal correlation between bins, hence the uncertainty on $\alpha_s(M_Z)$ will be roughly as large as the smallest systematic uncertainty on the measurement and the error might be overestimated.

As in the case of the inclusive jet cross section, the $\alpha_s(M_Z)$ uncertainty due to PDFs is determined by fitting the theory obtained with the formula (3.27), more precisely the upper and lower bound of the shaded region in Fig. 6.3. Similarly we estimate the scale uncertainty performing the fit for renormalization and factorization scale variations by a factor of two $\mu_r = \mu_f = 0.5, 2p_T^{max}$.

The extracted value of the running coupling constant evaluated at the mass of the Z^0 boson reads

$$\alpha_s(M_Z) = 0.1236 \pm 0.0002(stat.) \pm 0.0044(syst.)^{+0.0062}_{-0.0067}(PDF)^{+0.0061}_{-0.0024}(scale). \qquad (6.6)$$

The value of α_s is within uncertainties in an agreement with the world average (1.1) $\alpha_s(M_Z) = 0.1176 \pm 0.0020$. The theoretical PDF and scale uncertainties are of about the

measurement	$\alpha_s(M_Z)$	stat.	syst.	PDF	scale	total
$D\emptyset_{dijet}$	0.1236	$< 0.1\%$	4%	$^{+5\%}_{-5\%}$	$^{+5\%}_{-2\%}$	$\sim$ 8%
$D\emptyset_{incl}$	0.1212	$< 0.1\%$	6%	$^{+8\%}_{-6\%}$	$^{+4\%}_{-0\%}$	$\sim 10\%$
CDF_{incl}	0.1178	$< 0.1\%$	$^{+7\%}_{-8\%}$	$\pm 5\%$	$^{+6\%}_{-4\%}$	$\sim 10\%$
LEP	0.1202	$< 0.1\%$	1%	total. teor. 4%		4%

Table 6.1: The summary $\alpha_s(M_Z)$ extraction from inclusive jet production and dijet angular decorrelation measurements at DØ, inclusive jet production at CDF, plus the LEP measurement of event shapes.

same order. They play the major role in the uncertainty on $\alpha_s(M_Z)$. The quality of the fit was $\chi^2/\text{d.o.f} = 2.2$.

6.3 Results Summary

Here we provide a summary of $\alpha_s(M_Z)$ determination from the inclusive jet cross section and dijet azimuthal decorrelation. One important property that distinguishes the two DØ measurements is their dependence on the strong coupling constant. Whereas in LO the jet production is proportional to α_s^2, it is a function of α_s only in case of the $\Delta\phi$ distribution. This difference notably influences the contribution of various uncertainties on $\alpha_s(M_Z)$. The summary of all the considered DØ, CDF and LEP results is review in Tab. 6.1.

First we observe that both the DØ measurements suffer from the uncertainty approximately more than two times higher than the LEP measurement. The dependence on the PDF was reduced in the case of the $\Delta\phi$ distribution which we explained as a consequence of the particular definition of the observable as a cross section ratio. Since the jet production is proportional to α_s^2, the error of the measurement which was about 16% for E_T close to 200 GeV propagated to the uncertainty on $\alpha_s(M_Z)$ with half of the error. Therefore the PDF uncertainty on $\alpha_s(M_Z)$ from both measurements is comparable at the end.

From the Tab. 1 we see that the $\Delta\phi$ is slightly a better observable for the determination of the strong coupling constant. Moreover, the measurement was performed at the beginning of the Run II at the Tevatron. At that time, the jet energy calibration was known with roughly twice as worse precision than today. The determination of the coupling constant from the dijet azimuthal decorrelation measured at DØ today would yield the systematic uncertainty of $\alpha_s(M_Z)$ approximately 2%, bringing the total uncertainty down to about $6-7\%$. Even though the precision 4% obtained from the LEP experiment will not be overcome, the hadron-hadron colliders can approach it.

The possible way to do more precise α_s measurement would be to check other 3-jet observables for their predictive power. An example might be the 3-jet to 2-jet production ratio. Looking in the future, it would be interesting to study the observable in pp collisions

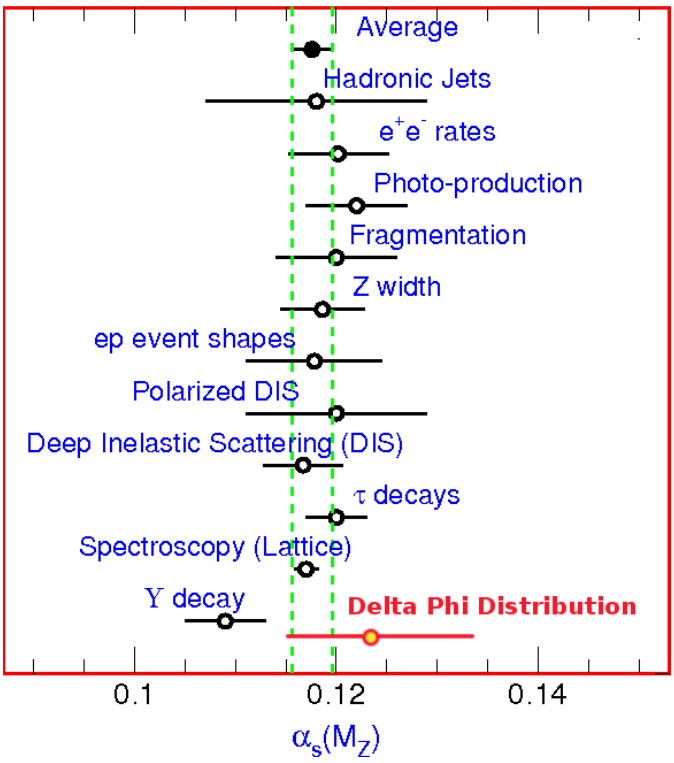

Figure 6.9: $\alpha_s(M_Z)$ extracted from various experiments. The α_s measurement from $\Delta\phi$ is included on the bottom.

relevant for LHC, where much higher transverse momenta will be achieved and the α_s running will be possible to test in a new momentum domain.

We conclude this chapter by compiling our result to the set of experiments also used for the extraction of α_s. Fig. 6.9 shows that the result from $\Delta\phi$ distribution is compatible with the world average.

Chapter 7

Conclusion

In this thesis, we analyzed two DØ measurements in order to extract the coupling constant of the strong interaction. We got accustomed to the techniques needed to get a prediction of any 2-jet or 3-jet IR-safe observable in NLO with computer programs NLOJET++ and fastNLO.

First, we calculated the inclusive jet cross section as a 2-jet observable in NLO, compared it with the measured data, and used it for the determination of strong coupling constant $\alpha_s(M_Z)$. The results provided us with the information that α_s determination from the inclusive jet cross section suffers the most from the uncertainty on parton distribution functions involved in the theoretical calculation, and from the uncertainty on the jet energy calibration.

Later, we turned our attention to the analysis of dijet azimuthal decorrelation measurement with the aim to determine the strong coupling more precisely than from the inclusive jet cross section. There we had to use the new 3-jet NLO calculation to satisfactory describe data. With this observable we experienced the cancellation of experimental systematics and also of the parton distribution function uncertainties, hence the $\Delta\phi$ distribution could be used to determine $\alpha_s(M_Z)$ more precisely than from the inclusive jet cross section where the total uncertainty was roughly 10%. We obtained the value of the strong coupling constant

$$\alpha_s(M_Z) = 0.1236 \pm 0.0002(stat.) \pm 0.0044(syst.)^{+0.0062}_{-0.0067}(PDF)^{+0.0061}_{-0.0024}(scale).$$

With the present jet energy calibration of the DØ detector, it would be possible to determine the $\alpha_s(M_Z)$ even more precisely, with an error of $6-7\%$. This is a significant improvement of error on α_s extracted from hadron colliders; however, it is still quite away from the LEP measurement which has the precision of 4%. Further improvements of precise α_s measurement might be possible with a better choice of 3-jet observable which will be less sensitive to the parton distribution functions and to experimental systematics.

QCD Formulas

The following notation is used:

1. Greek indices $\alpha, \beta, \gamma \ldots$ dentote the components of Lorentz tenzors.
2. $i, j, k, l = 1 \ldots 3$ are the color indices.
3. $\mathrm{a}, \mathrm{b}, \mathrm{c}, \mathrm{d}, \mathrm{e} = 1 \ldots 8$ represent gluon color indices.
4. g_s is the strong coupling constant.
5. n_f states the number of flavors. N is the number of colors.

A.1 QCD Lagrangian and SU(3) Matrix Representation

QCD classical Lagrangian, describing the interaction of quarks and gluons, is

$$\mathcal{L} = -\frac{1}{4}(F^a_{\mu\nu}F^{\mu\nu,a})^2 + \sum_{\text{flavors}} \bar{\psi}(\mathrm{i}\not{D} - m)\psi. \tag{A.1}$$

Here ψ is the quark field, $D^{\mu\nu}$ is the covariant derivative shown below, and $F^a_{\mu\nu}$ is the field strength tensor of the gluon filed A^a_m constructed as

$$F^a_{\mu\nu} = \partial_\mu A^a_\nu - \partial_\nu A^a_\mu - g_s f^{abc} A^b_\mu A^c_\nu. \tag{A.2}$$

The f^{abc} coefficients are the structure constants of the $SU(3)$ group. They are antisymmetric in indexes $a, b, c = 1 \ldots 3$ and obey the Jacobi identity

$$f^{abe}f^{ecb} + f^{cbe}f^{aed} + f^{dbe}f^{ace} = 0. \tag{A.3}$$

The covariant derivative is a matrix in the color space, and has the form

$$(D_\mu)_{ij} = \partial_\mu \delta_{ij} + \mathrm{i}g_s(t^a A^a_\mu)_{ij}, \tag{A.4}$$

when acting on the quark fields, and the form

$$(D_\mu)_{ab} = \partial_\mu \delta_{ab} + \mathrm{i}g_s(T^c A^c_\mu)_{ab}, \tag{A.5}$$

when acting on the gluon fields. The (3x3) matrices t^a and (8x8) matrices T^a are the generators of $SU(3)$ in the fundamental representation F and adjoint representation A, respectively. They satisfy the basic commutation relations,

$$[t^a, t^b] = \mathrm{i} f^{abc} t^c, \quad [T^a, T^b] = \mathrm{i} f^{abc} T^c, \tag{A.6}$$

$$(T^a)_{bc} = -\mathrm{i} f^{abc}. \tag{A.7}$$

Conventionally, the generator matrices for any $SU(N)$ are normalized as

$$\mathrm{Tr}(t^a t^b) = C(F)\delta^{ab}, \quad C(F) = \frac{1}{2}, \tag{A.8}$$

and they satisfy relations

$$t^a_{ij} t^a_{kl} = \frac{1}{2}\left[\delta_{il}\delta_{jk} - \frac{1}{N}\delta_{ij}\delta_{kl}\right], \tag{A.9}$$

$$t^a_{ij} t^a_{jl} = C_2(F)\delta_{il}, \quad C_2(F) = \frac{N^2-1}{2N}. \tag{A.10}$$

Generators in adjoint representation obey

$$\mathrm{Tr}(T^a T^b) = f^{acd} f^{bcd} = C(A)\delta^{ab}, \quad C(A) = N, \tag{A.11}$$

$$T^a_{bc} T^a_{cd} = C_2(A)\delta_{cd}, \quad C_2(A) = N.$$

The anticomutator of generators t^a reads

$$\{t^a, t^b\} = \frac{1}{N}\delta^{ab}\cdot\mathbf{1} + d^{abc} t^c, \tag{A.12}$$

where the coeficients d^{abc} are totaly antisymetric objects satisfying

$$d_{abb} = 0, \quad d_{acd} d_{bcd} = \frac{N^2-4}{N}\delta_{ab}, \tag{A.13}$$

$$f_{abe} d_{ecd} + f_{cbe} d_{aed} + f_{dbe} d_{ace} = 0. \tag{A.14}$$

Using the symetric and antisymetric coeficients f^{abc}, d^{abc}, respectively, it is simple to write down the expresion for the trace of three generators t^a. It reads

$$\mathrm{Tr}(t^a t^b t^c) = \frac{1}{4}(d^{abc} + \mathrm{i} f^{abc}). \tag{A.15}$$

A.2 QCD Feynman Rules

The Feynamn rules for QCD vertices are summarized in Tab. A.1

The prescripton for the gluon propagator depends on the choice of gauge. In the *covariant gauges* the gauge fixing term in the Lagrangians reads

$$\mathcal{L}_{\mathrm{gf}} = -\frac{1}{2\eta}(\partial_\mu A^\mu)^2, \tag{A.16}$$

$ig_s(t^a)_{ij}(\gamma^\mu)_{\alpha\beta}$	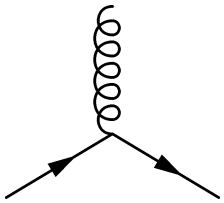
$-g_s f^{abc}[g^{\alpha\beta}(p-q)^\gamma + g^{\beta\gamma}(q-r)^\alpha + g^{\gamma\alpha}(r-p)^\beta]$ all momenta outgoing	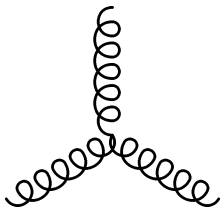
$-ig_s^2\{f_{eac}f_{ebd}[g^{\alpha\beta}g^{\gamma\delta} - g^{\alpha\delta}g^{\beta\gamma}]$ $+f_{ead}f_{ebc}[g^{\alpha\beta}g^{\gamma\delta} - g^{\alpha\gamma}g^{\beta\delta}]$ $+f_{eab}f_{ecd}[g^{\alpha\gamma}g^{\beta\delta} - g^{\alpha\delta}g^{\beta\gamma}]\}$	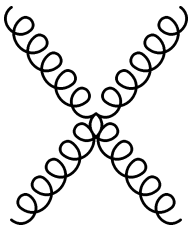

Table A.1: Vertex diagrams in QCD

where η is an arbitrary parameter. This class of gauges requires the introduction of ghost fields in order to obtain gauge invariant cross section; however the propagator is relatively simple with this choice:

$$\Gamma^{ab}_{\alpha\beta} = \delta^{ab}\left[-g_{\alpha\beta} + (1-\eta)\frac{p_\alpha p_\beta}{p^2+\mathrm{i}\epsilon}\right]\frac{\mathrm{i}}{p^2+\mathrm{i}\epsilon}. \tag{A.17}$$

With the special choice of $\eta = 1$ (*Feynman gauge*), the gluon propagator becomes equal to the foton propagator times the color factor δ^{ab}. Another special choice is $\eta = 0$ (Landau gauge).

The class of *axial gauges* is defined by a gauge fixig Lagrangian

$$\mathcal{L}_{\mathrm{gf}} = -\frac{1}{2\eta}(n_\mu A^\mu_a)^2, \tag{A.18}$$

where n is an arbitrary four vector. There is no need to introduce ghosts, but the gluon propagator becomes more complicated

$$\Gamma^{ab}_{\alpha\beta}(p) = \delta^{ab}\left[-g_{\alpha\beta} + \frac{n_\alpha p_\beta + p_\alpha n_\beta}{n\cdot p} - \frac{(n^2+\eta p^2)p_\alpha p_\beta}{(n\cdot p)^2}\right]\frac{\mathrm{i}}{p^2+\mathrm{i}\epsilon}. \tag{A.19}$$

In particular, the choice $\eta = 0$ and $n^2 = 0$ corresponds to the so-called *light-cone gauges*. It reduces the form of the gluon propagator to

$$\Gamma^{ab}_{\alpha\beta}(\partial) = \delta^{ab}\left[-g_{\alpha\beta} + \frac{n_\alpha p_\beta + p_\alpha n_\beta}{n\cdot p}\right]\frac{\mathrm{i}}{p^2+\mathrm{i}\epsilon}. \tag{A.20}$$

In the limit $p^2 \to 0$ one finds

$$n^\alpha \Gamma^{ab}_{\alpha\beta} = p^\alpha \Gamma^{ab}_{\alpha\beta} = 0, \tag{A.21}$$

hence only two physical polarization states ortogonal to p and n propagate. In this limit, the gauge is called *physical gauge*. The sum over the two gluon polarizateion states λ is

$$\sum_\lambda \epsilon^\alpha_\lambda \epsilon^{\star\beta}_\lambda = -g^{\alpha\beta} + \frac{n_\alpha p_\beta + p_\alpha n_\beta}{n\cdot p} = -g^{\alpha\beta}_\perp. \tag{A.22}$$

Bibliography

[1] S. Eidelman et al., Phys. Lett. B 592, 1 (2004) and 2005 partial update for the 2006 edition available on the PDG WWW pages (URL: http://pdg.lbl.gov/)

[2] S. Bethke, Nucl. Phys. Proc. Suppl. **135** (2004) 345 [arXiv:hep-ex/0407021].

[3] LEP Collaboration – QCD group, *http://lepqcd.web.cern.ch/LEPQCD/annihilations/alphas_jun04/index.html*, June 15, 2004.

[4] F. Abe *et al.* [CDF Collaboration], Phys. Rev. Lett. **68** (1992) 1104.

[5] Z. Nagy, *nlojet++ home page*, http://www.cpt.dur.ac.uk/ nagyz/nlo++/

[6] V. M. Abazov *et al.* [D0 Collaboration], Phys. Rev. Lett. **94** (2005) 221801 [arXiv:hep-ex/0409040].

[7] B. Abbott *et al.* [D0 Collaboration], Phys. Rev. Lett. **86** (2001) 1707 [arXiv:hep-ex/0011036].

[8] Ta-Pei Cheng, Ling-Fong Li, *Gauge theory of elementary particle physics*, Oxford University Press, New York, 1984

[9] J. Pumplin, D. R. Stump, J. Huston, H. L. Lai, P. Nadolsky and W. K. Tung, JHEP **0207** (2002) 012 [arXiv:hep-ph/0201195].

[10] M. E. Peskin, D. V. Schroeder, *An Introduction to Quantum Field Theory* , Perseus Books, Cambridge, Massachusetts, 1995.

[11] R. K. Ellis, W. J. Stirling, B. R. Webber, *QCD and Collider Physics*, Cambridge University Press, Cambridge, 1996.

[12] T. van Ritbergen, J. A. M. Vermaseren and S. A. Larin, Phys. Lett. B **400** (1997) 379 [arXiv:hep-ph/9701390].

[13] J. Chýla, *Quarks, partons and Quantum Chromodynamics*, Lecture notes, http://www-hep2.fzu.cz/ chyla/talks/mytalks/lecture.pdf 2005.

[14] E. Busat, B. Andrieu, DØ Internal Note 4457, *Jet Algorithms in the DØRun II Software*, 2004.

[15] J.E. Huth, *et. al.* FERMILAB-CONF-90-249-E

[16] A. Kupčo, Measurement and QCD analysis of inclusive dijet mass cross section in $\bar{p}p$ collisions, Doctoral thesis, (2003).

[17] T. Sjostrand, P. Eden, C. Friberg, L. Lonnblad, G. Miu, S. Mrenna and E. Norrbin, Comput. Phys. Commun. **135** (2001) 238 [arXiv:hep-ph/0010017].

[18] Z. Nagy and Z. Trocsanyi, Phys. Rev. Lett. **87** (2001) 082001 [arXiv:hep-ph/0104315].

[19] Z. Nagy, Phys. Rev. Lett. **88** (2002) 122003 [arXiv:hep-ph/0110315].

[20] Z. Nagy Phys. Rev. D **68** (2003) 094002 [arXiv:hep-ph/0307268].

[21] Z. Nagy and Z. Trocsanyi, Phys. Rev. Lett. **79** (1997) 3604 [arXiv:hep-ph/9707309].

[22] T. Kluge, K. Rabbertz, M. Wobisch, fastNLO, http://hepforge.cedar.ac.uk/fastnlo/, 2001.

[23] M. L. Mangano, P. Nason and G. Ridolfi, Nucl. Phys. B **373** (1992) 295.

[24] P. Aurenche, R. Baier, M. Fontannaz and D. Schiff, Nucl. Phys. B **297** (1988) 661.

[25] T. Affolder *et al.* [CDF Collaboration], Phys. Rev. Lett. **88** (2002) 042001 [arXiv:hep-ex/0108034].

[26] P. M. Stevenson, Phys. Rev. D **23** (1981) 2916.

[27] G. Grunberg, Phys. Rev. D **29** (1984) 2315.

[28] S. J. Brodsky, G. P. Lepage and P. B. Mackenzie, Phys. Rev. D **28** (1983) 228.

[29] *The Durham HEP Databases*,
Durham University(UK), http://durpdg.dur.ac.uk/HEPDATA/

[30] I. A. Bertram, Internal DØNote 3644, *A Study of the* $\chi 2$ *Comparisons Used in the Inclusive Jet Analyses*, 1999.

[31] R. W. L. Jones, M. Ford, G. P. Salam, H. Stenzel and D. Wicke, JHEP **0312** (2003) 007 [arXiv:hep-ph/0312016].

[32] J. Pumplin, private communication, J. Pumplin, D. R. Stump, J. Huston, H. L. Lai, P. Nadolsky and W. K. Tung, JHEP **0207**, 012 (2002) [arXiv:hep-ph/0201195].

D. Stump, J. Huston, J. Pumplin, W. K. Tung, H. L. Lai, S. Kuhlmann and J. F. Owens, JHEP **0310**, 046 (2003) [arXiv:hep-ph/0303013].

[33] A. Kupčo, M. Begel, P. Demine, Ch. Royon, M. Wobisch, M. Zielinski, DØ Internal Note 4384 – Measurement of Dijet Azimuthal Angle Distribution in $p\bar{p}$ collisions at $\sqrt{s} = 1.96$ TeV, 2004.